Glutathione-mediated biotransformation in the liver modulates nanoparticle transport

Supplementary Information

Xingya Jiang, Bujie Du and Jie Zheng*

Department of Chemistry and Biochemistry, The University of Texas at Dallas, 800 West Campbell Road, Richardson, Texas 75080, USA
*Corresponding email: jiezheng@utdallas.edu

Table of Contents

1.Materials and Methods

1.1 Materials and equipment

ICG-NHS was purchased from Intrace Medical (Switzerland) while all the other chemicals were obtained from Sigma-Aldrich (USA) and used as received unless specified. Four distinct-sized bare AuNPs (citrate protected) and Clodronate liposomes (Clophosome) were purchased from NanoComposix, Inc (USA) and FormuMax Scientific, Inc (USA), respectively. The related absorption spectra were measured with a Virian 50 Bio UV-Vis spectrophotometer. Fluorescence spectra were acquired with a PTI QuantaMasterTM 30 fluorometer. The core size and hydrodynamic diameter of nanoparticles were measured 200kV JEOL 2100 transmission electron microscope and Malvern ZS90 particle size analyzer. In vivo fluorescence images were recorded using a Carestream In-Vivo FX Pro imaging system. Optical imaging of cultured cells and tissue slides was obtained with an Olympus IX-71 inverted fluorescence microscope coupled with Photon Max 512 CCD camera (Princeton Instruments). Electron microscopic images of cultured cells were acquired using a 120 kV Tecnai G^2 spirit transmission electron microscope (FEI) equipped with a LaB_6 source. Shimadzu Prominence Modular HPLC equipped with UV-Vis detector (SPD-20A) and fluorescence detector (RF-20A) was used for the separation of derivatized thiol ligands. Agarose gel electrophoresis was carried out in a Bio-Rad Mini-Sub Cell GT system. Agilent 7900 inductively coupled plasma mass spectrometry (ICP-MS) was used for the quantitative analysis of Au in biological samples. Human breast cancer MCF-7 cell line was used for *in vitro* cell study and *in vivo* xenograft model as well. Animal studies were performed according to the guidelines of the University of Texas System Institutional Animal Care and Use Committee. BALB/c mice (strain code 047, 6–8 weeks old, weighing 20–25 g) were purchased from Envigo. All mice were randomly allocated and housed under standard environmental conditions (23±1°C, 50±5% humidity and a 12/12h light/dark cycle) with free access to water and standard laboratory food.

1.2 Synthesis of GS-Au25 ($Au_{25}(SG)_{18}$) and ICG-GS-Au25 conjugates.

Atomically monodisperse $Au_{25}(SG)_{18}$ nanoclusters were synthesized according to the reported method[4]. Characterization of the synthesized $Au_{25}(SG)_{18}$ can be found in Supplementary Fig. 1. For the synthesis of ICG_4-GS-Au25, 4mg ICG-NHS (dissolved in DMSO) was added into 6mg GS-Au25 aqueous solution and the mixture was vortexed for 3h. Then ICG-GS-Au25 conjugates were purified after removing unconjugated ICG dye through centrifugation in the presence of ethanol. The conjugates were again redispersed in 1X PBS buffer and purified by Amicon Ultra centrifuge filters to remove any unconjugated GS-Au25 nanoclusters. The resulting ICG_4-GS-Au25 inside the centrifuge filter was resuspended in ultrapure water and lyophilized for future usage. For the synthesis of GS-Au25 conjugated with fewer number of ICG molecules, reduced feeding ratios of ICG-NHS/GS-Au25 were adopted and the products were purified following the same protocol as that of ICG_4-GS-Au25. Additional characterization of the synthesized ICG_4-GS-Au25 is in Supplementary Fig. 2.

1.3 Synthesis of different-sized ICG/PEG-AuNPs, MBA-AuNPs and GS-Au polymeric nanoparticles

Different-sized ICG/PEG-AuNPs were obtained by surface-ligand exchange of different-sized bare AuNPs with ICG-GSH and PEG-SH (average molecular weight ~2000) in water for 1h at 55°C under vigorous stirring. The resulting ICG/PEG-AuNPs were purified by gel filtration column to remove free ICG-GSH and PEG-SH. The 4-mercaptobenzoic acid (MBA) coated AuNPs (MBA-AuNPs) were synthesized by adding 1M $HAuCl_4$ aqueous solution to 10mM MBA solution containing 50% (v/v) methanol at a molar ratio of 1:3. The mixture was first stirred at room temperature for 15 min and then brought to 0°C in

ice cold water followed by introducing ice cold 150mM $NaBH_4$ aqueous solution with a $NaBH_4$: $HAuCl_4$ molar ratio of 2:1. The reaction was further proceeded for another 30min and dark MBA-AuNPs were collected by centrifugation. Large and small MBA-AuNPs were obtained by 25% native polyacrylamide gel electrophoresis (PAGE) separation of the synthesized MBA-AuNPs. The ~100 nm (HD) GS-Au polymeric nanoparticles were synthesized by adding 1M $HAuCl_4$ aqueous solution to GSH aqueous solution (~12mM) at a molar ratio of 1:3 with gentle stirring. Colorless GS-Au polymer precipitates were formed subsequently and collected by centrifugation. The precipitates were redispersed in water and freeze dried to yield GS-Au polymeric nanoparticles. Conjugation of ICG to GS-Au polymeric nanoparticles were performed in a similar way to that of GS-Au25 using amine-reactive ICG-NHS.

1.4 Synthesis of ICG-GSSG, ICG-GSH, ICG-Cis-Pt prodrug

ICG-GSSG conjugates were synthesized by mixing ICG-NHS (dissolved in DMSO) and GSSG (glutathione oxidized, dissolved in water) at a molar ratio of 1:5 and ~pH 8. The reaction proceeded for 2h under agitation and ICG-GSSG could be purified by acetone-induced precipitation and subsequent dialysis against ultrapure water. ICG-GSH was facilely obtained by reducing ICG-GSSG with TCEP (tris(2-carboxyethyl)phosphine) in aqueous solution. ICG-Cis-Pt prodrug was synthesized by linking the primary amine group of ICG-GSSG with the carboxyl group of Cis-Pt prodrug through a typical EDC/NHS coupling reaction. The mono-carboxylated Cis-Pt prodrug (cis,cis,trans-[Pt(NH3)2Cl2(OH)(O2CCH2CH2COOH)]) was synthesized according to the reported protocol[5].

1.5 Quantification of the number of ICG molecules per GS-Au25 nanocluster

The purified ICG-GS-Au25 conjugates were dissolved in ultrapure water containing 20mM cysteine (pH adjusted to 7.4 by NaOH) and incubated for 30 min (protected from light exposure) to completely release ICG from Au25 surface (see Supplementary Fig. 3), then ICG concentration was quantified by its characteristic absorption peak at 780nm and a pre-established concentration vs. absorption standard curve while the Au25 concentration was quantified by ICP-MS analysis of the Au content.

1.6 Depletion of tissue GSH in vivo

The temporary depletion of tissue GSH was achieved by a single injection of diethyl maleate (DEM). DEM was intraperitoneally administered into BALB/c mice at a dose of 1mL/kg body weight ~40 min prior to the injection of ICG_4-GS-Au25 or other probes. The success of tissue GSH depletion was verified by the rapid decrease in plasma GSH level following DEM administration (Supplementary Fig. 10). A single injection of DEM decreased plasma GSH level down to ~12% of the initial value (~30 μM) and maintained this low GSH level for ~2-3 h before the gradual recovery of plasma GSH, consistent with the literatures[6,7]. Quantification of GSH was carried out by a modified Tietze enzymatic recycling assay established previously[8].

1.7 In vivo fluorescence imaging of ICG_4-GS-Au25

Hair-removed BALB/c mice (~25 g/mouse) were pretreated with PBS, DEM (1mL/kg body weight), Clophosome (7mg/mL clodronate disodium, 200uL/mouse as recommended by the manufacturer) and control liposomes, respectively. Then under 3%

isoflurane anesthesia, mouse was tail-vein catheterized and prone-positioned on the imaging stage. 150μL ICG_4-GS-Au25 (20μM, in PBS) was tail vein injected following by a sequential time-series imaging collection. The fluorescence imaging parameters were set as follow: EX760nm/EM830nm; 10s exposure time; 2x2 binning.

1.8 Quantification of the average number of ICG molecules per circulating Au25 nanocluster

Blood samples (~30μL) from BALB/c mice were collected retro-orbitally at different time points after i.v. injection of ICG_4-GS-Au25. Immediately after each collection, blood sample was mixed with 100μL ice cold PBS buffer containing 2% EDTA and centrifuged at 1200g for 5min to precipitate blood cells. Then the supernatant was equally divided into two aliquots and 100μL PBS or dithiothreitol (DTT, 20mM) PBS solution were added to each aliquot, respectively. After 15 min incubation, the ICG fluorescence of each aliquot was measured and the increase (dithiothreitol treated vs. PBS treated) in fluorescence intensity was normalized to Au amount (quantified by ICP-MS) for each time point. The percentage of ICG fluorescence increment per Au at each time point with respect to that of ICG_4-GS-Au25 dissolved directly in plasma (simulated as the 0 min time point) was used to calculate the average number of ICG molecules per circulating Au25. A scheme of these experiment procedure is included in Supplementary Fig. 13.

1.9 Pharmacokinetics and biodistribution study of ICG_4-GS-Au25

PBS or DEM pretreated BALB/c mice were i.v. injected with 150 μL ICG_4-GS-Au25 (~20μM, in PBS) per mouse. At certain time point post injection, blood sample (~30μL) was retro-orbitally collected and weighed, followed by the addition of 500μL lysis buffer containing 20mM dithiothreitol (pH~8) to liberate ICG from Au25 nanocluster and recover the quenched fluorescence of ICG. Then fluorescence of dithiothreitol treated blood sample was measured by the in vivo imaging system to quantify ICG in blood. Afterwards, the blood sample was completely dissolved in freshly made aqua regia and the Au amount in blood was analyzed by ICP-MS. Biodistribution of ICG_4-GS-Au25 in different organs/tissues was quantified in a similar way. Organs/tissues were collected and weighed following the sacrifice of mice and then completely digested in aqua regia to determine the Au content via ICP-MS. The ICG content in different organs/tissues was quantified by its NIR fluorescence after dissociation from Au25 by homogenizing organs/tissues in lysis buffer containing 20mM dithiothreitol (pH~8). Standard curves of ICG fluorescence vs. concentration were constructed in the respective control organ/tissue lysate.

1.10 Tissue slide imaging with an optical microscope

BALB/c mice were sacrificed at 10min following the i.v administration of 150μL/mouse ICG_4-GS-Au25, ICG-GSH, ICG or PBS, respectively. The liver and kidneys were then collected and fixed immediately in 10% neutral buffered formalin, followed by standard dehydration and paraffin embedding. The embedded tissues were then sectioned into 4 μm slices and H&E stained. The final slides were visualized under Olympus IX-71 fluorescence microscope equipped with ICG filters set (Chroma). Tumor tissues were obtained from BALB/c nude mice bearing MCF-7 xenograft tumors 24h after i.v. injection of ICG_4-GS-Au25 and processed with the same procedures as those for liver and kidney tissues. To visualize the gold nanoclusters in tumor tissues under bright-field optical microscope, silver staining was used to enhance their size and contrast. Tumor slides were first dewaxed in xylene and incubated in silver staining solution containing 0.05M $AgNO_3$ and 1mM hydroquinone for half an hour. Afterwards, tumor slides were washed with copious ultrapure water and dried in lab oven (65°C) for imaging under bright-field

of Olympus IX-71 microscope.

1.11 Fluorescent immunohistochemistry of liver tissue

Liver tissues from BALB/c mice i.v. injected with ICG_4-GS-Au25 were harvested at 10 min as well as 24 h p.i. and immediately fixed with 4% freshly prepared paraformaldehyde PBS solution for 2 h. Then the fixed liver tissues were immersed in 20% sucrose PBS solution overnight at 4°C before being embedded in freezing medium (OTC). The embedded liver tissues were sectioned into 5 μm-thickness slides in cryostat and blocked with PBS containing 5% normal goat serum for 1h at RT. Afterwards, liver slides were incubated with either rat anti-mouse F4/80 (Invitrogen) or 2.4G2 (CD16/CD32, BD Biosciences) primary antibodies in PBS containing 1% goat serum overnight at 4°C to stain macrophage or liver sinusoidal endothelial cell (LSEC), respectively. Primary antibody binding was visualized using goat anti-rat IgG secondary antibody conjugated with Alexa Fluor 647 (Invitrogen). Cell nuclei were counterstained with DAPI for 10 min before slides were mounted and subject to fluorescent microscopy.

1.12 Extract gold nanoparticles from the urine and blood samples for surface ligand analysis

The excreted AuNPs in the urine were purified first by adding 10% (m/v) 5-sulfosalicylic acid to precipitate urine proteins and followed by 10KDa centrifuge filter to separate AuNPs from the small molecules (urea etc.) presented in the urine. The separated AuNPs were further purified by 2% agarose gel electrophoresis and gel filtration column (Sephadex LH-20, GE Healthcare). The extraction of AuNPs in blood was similar to that in the urine. The blood from AuNPs injected mice was collected by cardiac puncture and centrifuged to obtain the plasma, then plasma protein was precipitated by adding 5-sulfosalicylic acid and the remaining AuNPs in supernatant were purified following the same protocol as we did for the urine. To extract sufficient AuNPs from the blood after circulation, renal arteries were clamped right before the i.v. injection of AuNPs in order to prevent the rapid blood elimination of ultrasmall AuNPs through the kidney filtration.

1.13 HPLC analysis of gold nanoparticle surface ligands

Toluene of 1mL was added to 500μL PBS containing purified AuNPs, then 2- pheylethanethiol was added to the top toluene layer and the mixture was vigorously stirred for 1-2h at room temperature to transfer gold cores to the organic phase while leaving the original hydrophilic ligands in the aqueous phase. Afterwards, TCEP was added to the PBS solution to reduce any disulfides formed in this process before HPLC analysis of the thiol ligands. A well-established NPM derivatization method[9] was used to quantitatively analyze the thiol ligands in PBS. The derivatives were separated by Shimadzu HPLC equipped with TSKgel column (Tosoh Bioscience) and fluorescence detector. The HPLC conditions were as follow: mobile phase 20/80 H_2O/MeCN containing 1ml/L acetic acid and 1ml/L phosphoric acid; isocratic flow 0.6ml/min; column temperature 25°C; detector wavelength EX330nm/EM380nm.

1.14 Statistics and reproducibility

Welch's *t*-test was used to compare two groups of data and analysis of variance (ANOVA) was used for the comparison of multiple data points among data sets. Data were reported as mean value with error bar representing the standard deviation.

Differences were considered statistically significant when $P < 0.05$. Unless otherwise specified, all of the experiments were repeated at least twice with similar results to ensure reproducibility.

2. Supplementary Figures

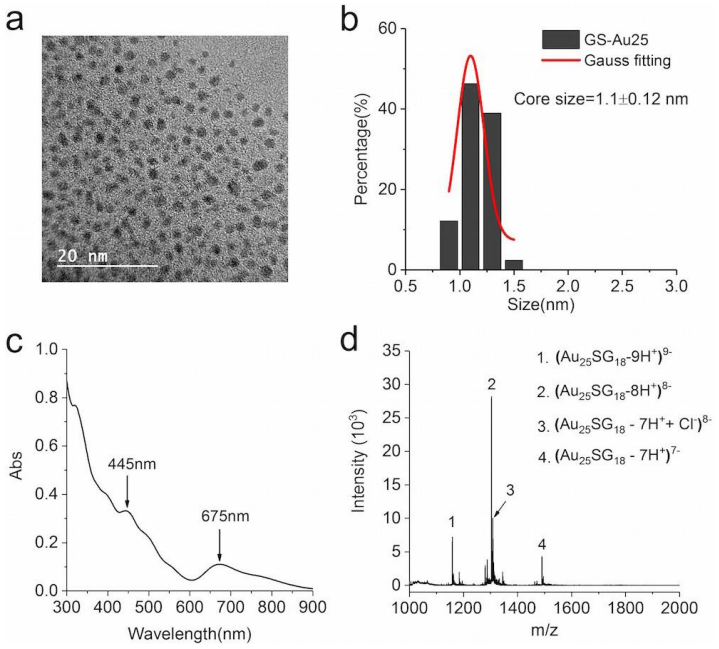

Supplementary Fig. 1. Characterization of the synthesized GS-Au25. (a) TEM image of the synthesized GS-Au25 nanoclusters. (b) The average core size of GS-Au25 is ~1.1 nm (1.1±0.12 nm, mean±sd, n=50 particles), comparable to that of the reported values[1]. (c) Absorption spectrum of the synthesized GS-Au25 exhibits the characteristic absorption features of Au25 nanoclusters. (d) Electrospray ionization mass spectrometry (ESI-MS) analysis confirms the molecular formula of $Au_{25}(SG)_{18}$. All the measurements were repeated three times with similar results.

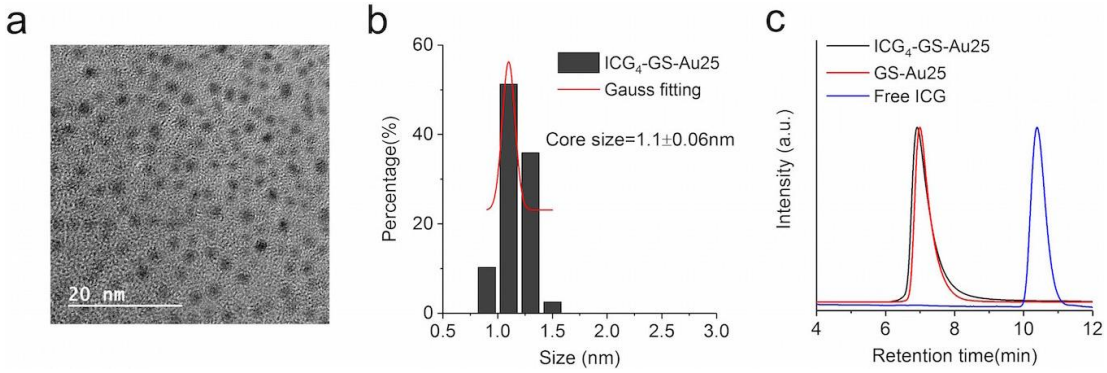

Supplementary Fig. 2. Characterization of ICG_4-GS-Au25. (a) TEM image of the purified ICG_4-GS-Au25 nanoprobes. (b) The average core size of ICG_4-GS-Au25 is ~1.1 nm (1.1±0.06 nm, mean±sd, n=50 particles), identical to that of GS-Au25. (c) Size-exclusion chromatography confirms that no free ICG was left after the purification of ICG_4-GS-Au25. All the measurements were repeated three times with similar results.

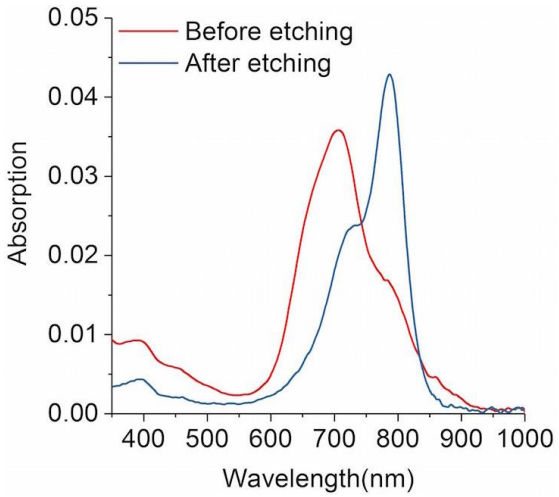

Supplementary Fig. 3. UV-Vis absorption of ICG$_4$-GS-Au25 before and after etching. After etching in 20mM cysteine (pH=7.4) for 30 min, ICG was completely detached from Au25 surface and showed its characteristic monomer absorption profile. This experiment was repeated four times with similar results.

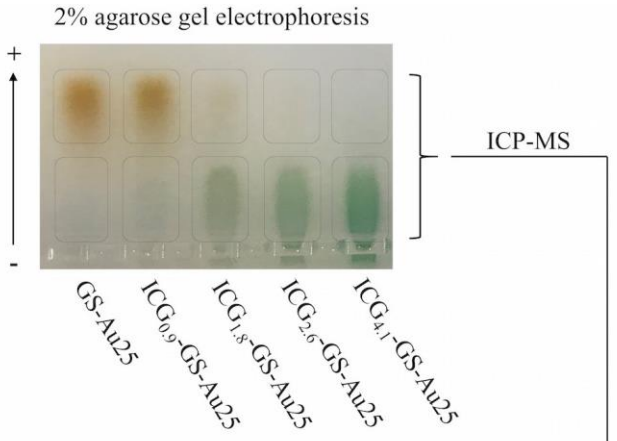

Average number of ICG per GS-Au25	0	0.9	1.8	2.6	4.1
Serum protein binding percentage	**2.5%**	**12.7%**	**66.2%**	**87.1%**	**97.4%**

Supplementary Fig. 4. Serum protein binding profiles of GS-Au25 conjugated with different numbers of ICG molecules. Serum protein binding percentage of each species was quantified by ICP-MS analysis of the Au content in corresponding gel bands (as circled by the dotted line). This experiment was repeated twice with similar results.

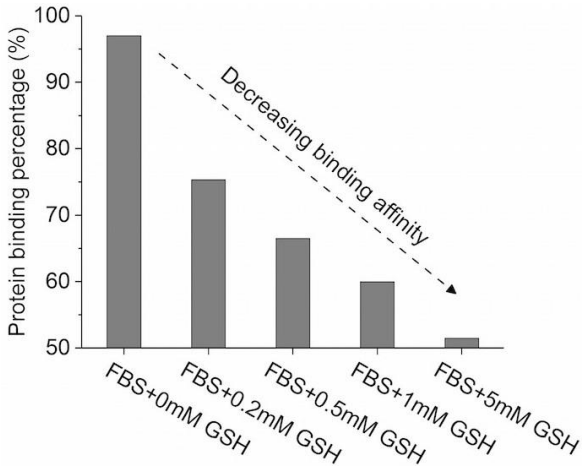

Supplementary Fig. 5. Serum protein binding profiles of ICG$_4$-GS-Au25 in various concentrations of GSH. ICG$_4$-GS-Au25 was mixed with FBS first and then added into PBS solutions containing different concentrations of GSH (pH=7.4). After 5 min incubation at 37^{o}C, protein binding and non-binding portions were separated by gel electrophoresis and quantified by ICP-MS.

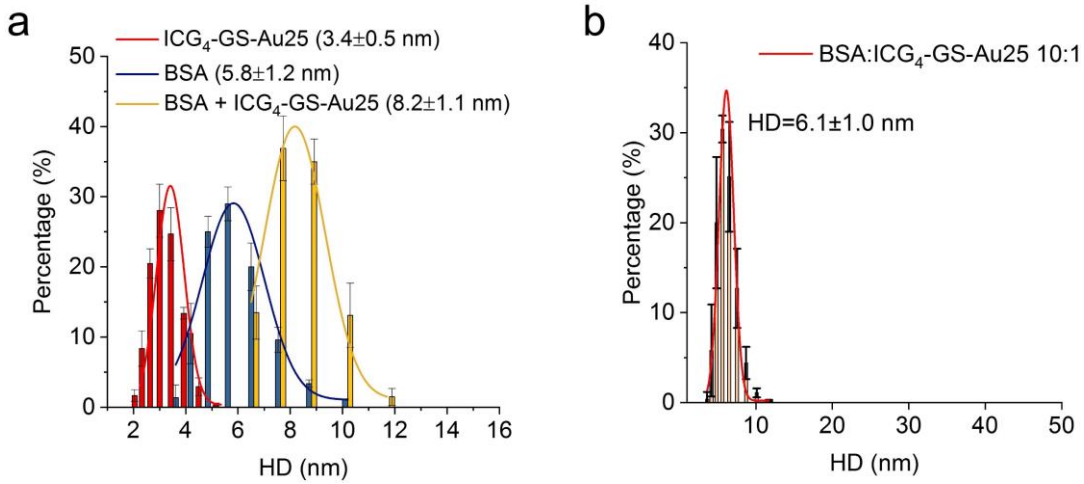

Supplementary Fig. 6. Hydrodynamic diameter (HD) of ICG$_4$-GS-Au25 in PBS and BSA. (a) In PBS, ICG$_4$-GS-Au25 has an HD of ~3.4 nm (n=3 measurements) whereas in the presence of BSA at molar ratio of 1:1, ICG$_4$-GS-Au25 binds to BSA and the overall HD increases to ~8.2 nm (n=3 measurements). (b) Large size aggregates were not observed by incubating ICG$_4$-GS-Au25 in excess of BSA (molar ratio 1:10), indicating that ICG$_4$-GS-Au25 will not aggregate in vivo after binding to serum proteins in blood. The measured size slightly decreased at 1:10 molar ratio due to the dominance of free BSA. Column values indicate the mean with error bars representing the standard deviation.

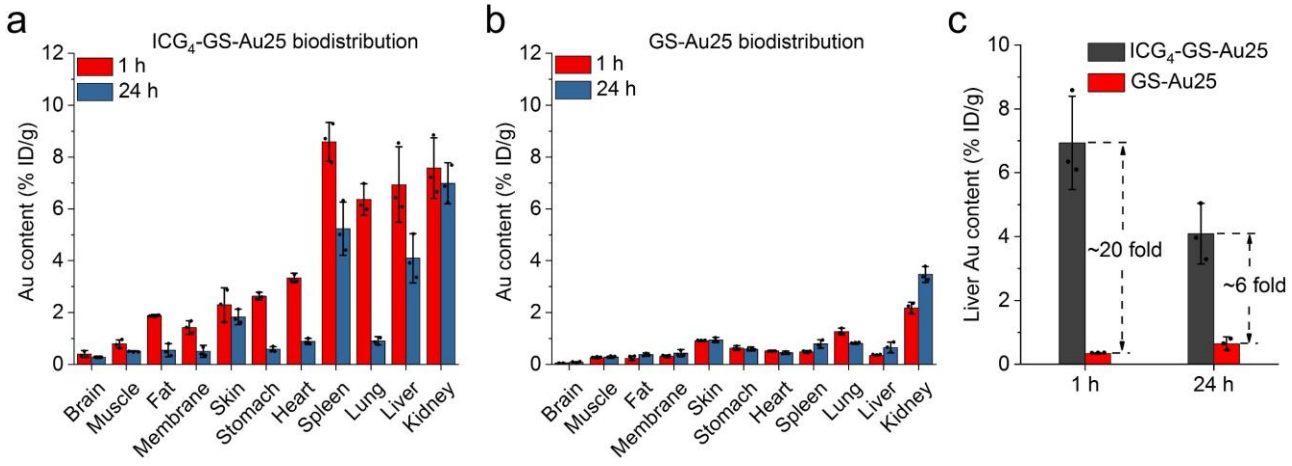

Supplementary Fig. 7. Biodistribution of ICG$_4$-GS-Au25 and GS-Au25 quantified by ICP-MS. (a), Au biodistribution in different organs of mice injected with ICG$_4$-GS-Au25 (n=3 mice). (b), Au biodistribution in different organs of mice injected with GS-Au25 (n=3 mice). (c) Comparison of Au content in liver (n=3 mice) at 1h and 24h p.i. Column values indicate the mean with error bars representing the standard deviation. These experiments were performed once with corresponding controls.

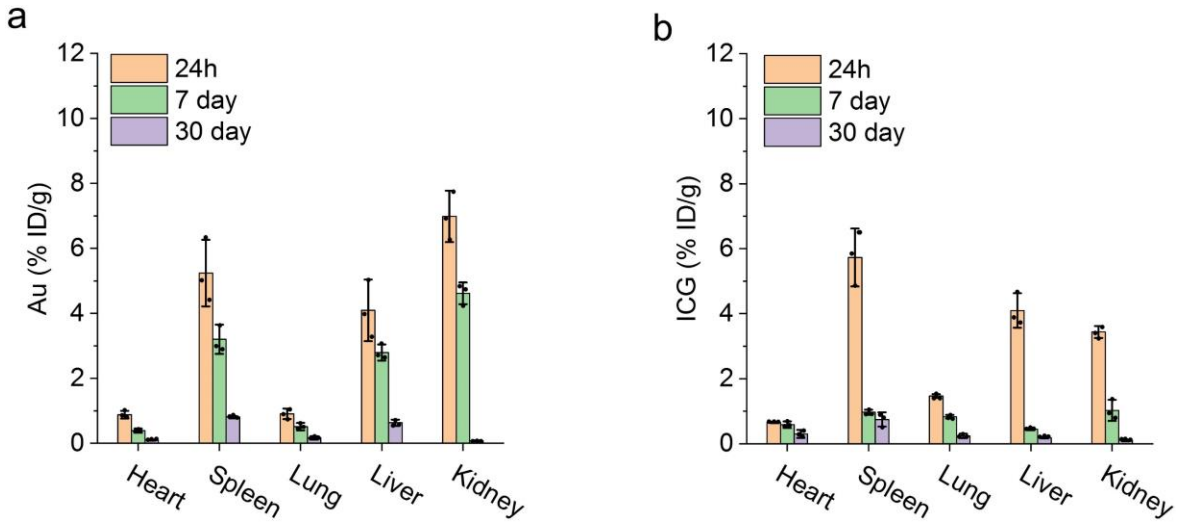

Supplementary Fig. 8. Long-term biodistribution of ICG$_4$-GS-Au25 in major organs. (a) Au biodistribution in major organs at 24h, 7day and 30 day after i.v. injection of ICG$_4$-GS-Au25 (n=3 mice). (b) ICG biodistribution in major organs at 24h (n=3 mice), 7day and 30 day after i.v. injection of ICG$_4$-GS-Au25 (n=3 mice). Column values indicate the mean with error bars representing the standard deviation. These experiments were performed once with corresponding controls.

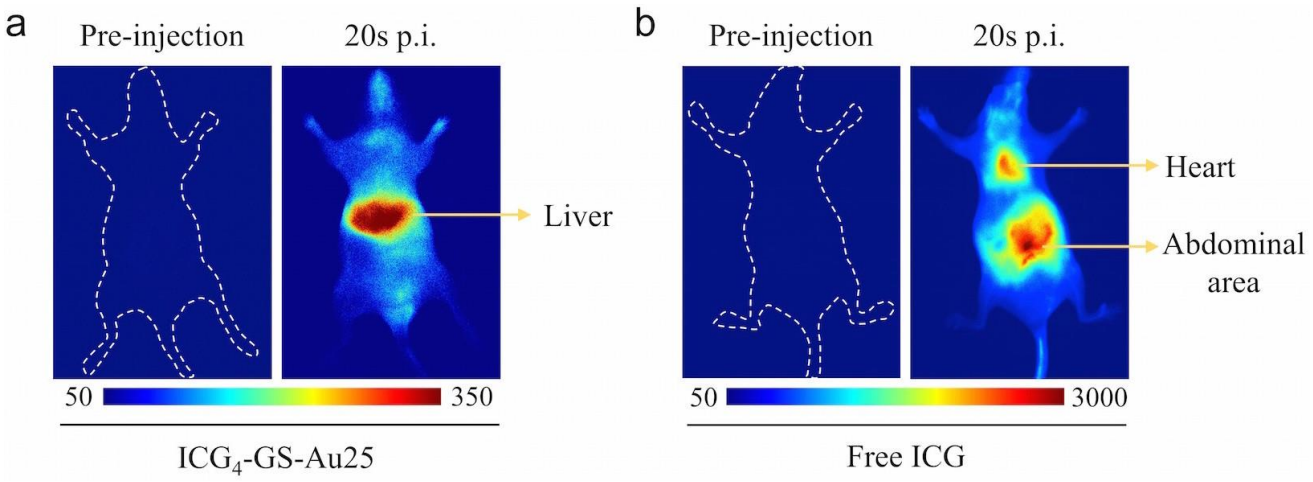

Supplementary Fig. 9. Representative in vivo fluorescence images of mice after intravenous injection of ICG_4-GS-Au25 and free ICG. Noninvasive in vivo fluorescence imaging of mice intravenously injected with ICG_4-GS-Au25 (a) and free ICG (b) at 20s post injection. Unlike free ICG that lighted up heart and background tissues (abdominal area) right after intravenous injection, ICG_4-GS-Au25 remained relatively dark during extra-hepatic blood circulation but was lighted up immediately after entering the liver, indicating the major role of liver in inducing the dissociation of ICG from Au25 in vivo. These experiments were repeated five times with similar results.

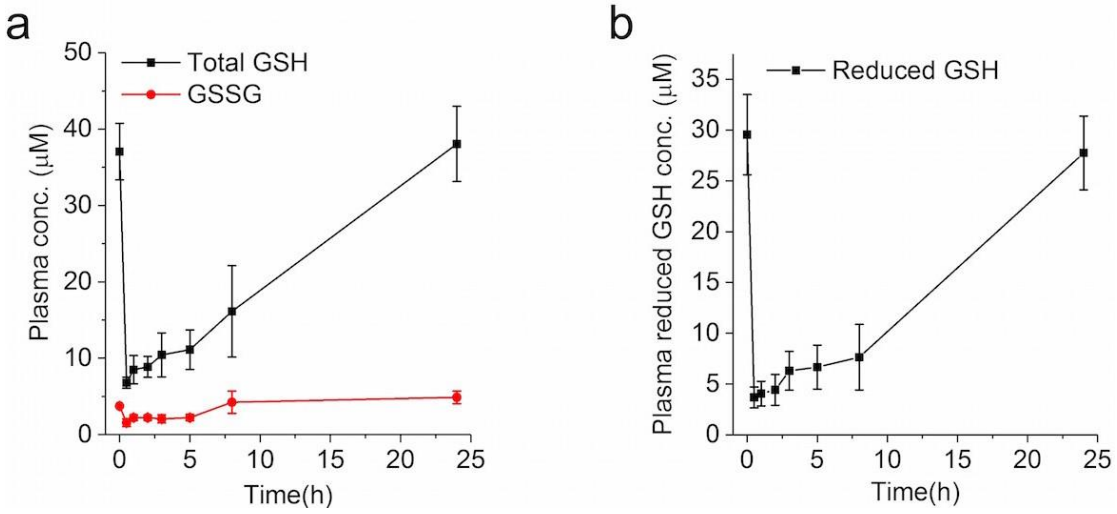

Supplementary Fig. 10. Plasma glutathione level after DEM administration. (a), Plasma total glutathione (reduced GSH + 2GSSG) and glutathione disulfide (GSSG) concentration at various time points after intraperitoneal injection of 1mL/kg DEM in mice (n=3 mice). (b), Plasma reduced glutathione concentration (n=3 mice) at different time was then calculated by subtracting GSSG from the total GSH concentration. The quantification of plasma total GSH and GSSG was carried out according to the established procedures (ref. 8) via a modified Tietze enzymatic recycling assay. Data points indicate the mean with error bars representing the standard deviation.

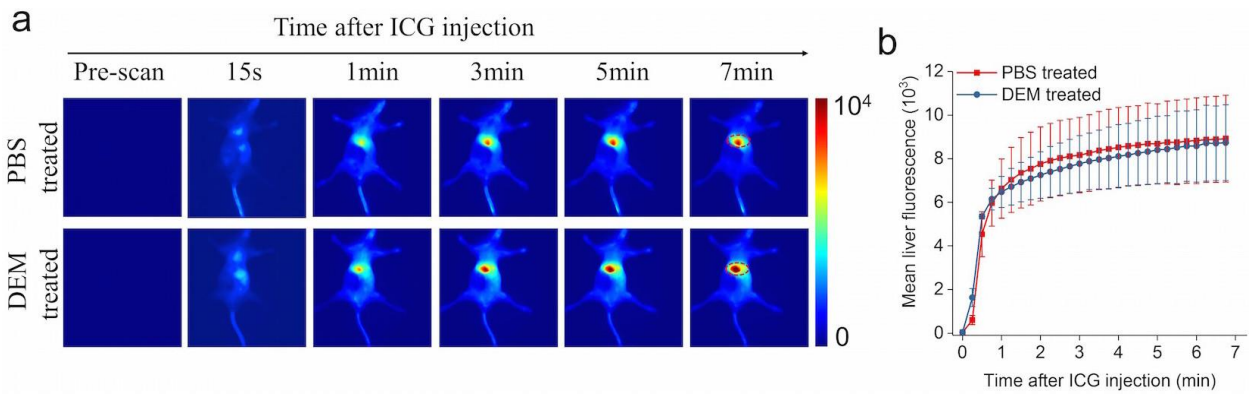

Supplementary Fig. 11. Comparison of liver uptake of ICG in DEM-treated mice and PBS-treated mice. (a) Representative time-series fluorescence images of DEM-treated and PBS-treated mice intravenously injected with the same amount of free ICG (~10 nmole). (b), Liver ICG fluorescence kinetics of PBS-treated (n=3) and DEM-treated (n=3) mice, indicating that hepatic uptake of ICG was not significantly altered after DEM administration. Red dashed circle indicates the region of interest (ROI) for liver fluorescence quantification. This experiment was performed once with corresponding controls. Data points indicate the mean with error bars representing the standard deviation.

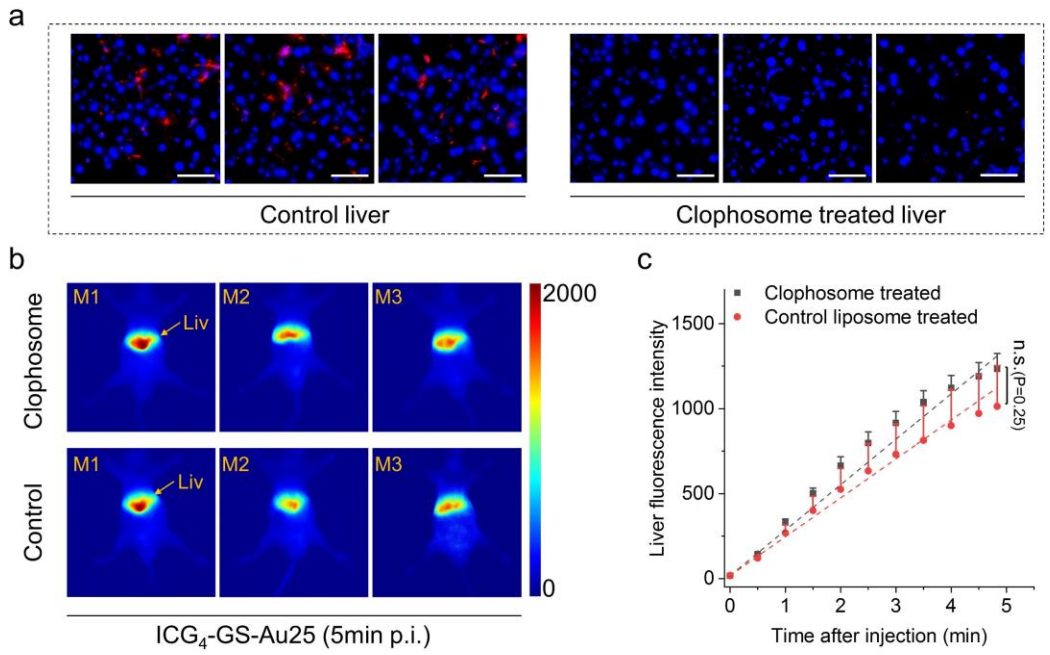

Supplementary Fig. 12. Noninvasive fluorescence imaging of ICG_4-GS-Au25 dissociation in macrophage-depleted mice and control mice. (a) Immunohistochemistry staining of liver tissues from control liposome treated mice (control) and clodronate liposomes (clophosome) treated mice (48h p.i.). Red channel, F4/80; blue channel, DAPI; scale bar, 40 μm. **(**b)Noninvasive *in-vivo* fluorescence images of mice (n=3 mice) pretreated with clophosome and control liposomes at 5min post i.v. injection of the same ICG_4-GS-Au25. (c) Liver ICG fluorescence kinetics of mice treated with clodronate liposomes (n=3 mice) and control liposomes (n=3 mice) after i.v. injection of the ICG_4-GS-Au25. These experiments were performed once with corresponding controls. Statistical significance is evaluated by two-way ANOVA ("n.s.", no significant difference). Data points indicate the mean with error bars representing the standard deviation.

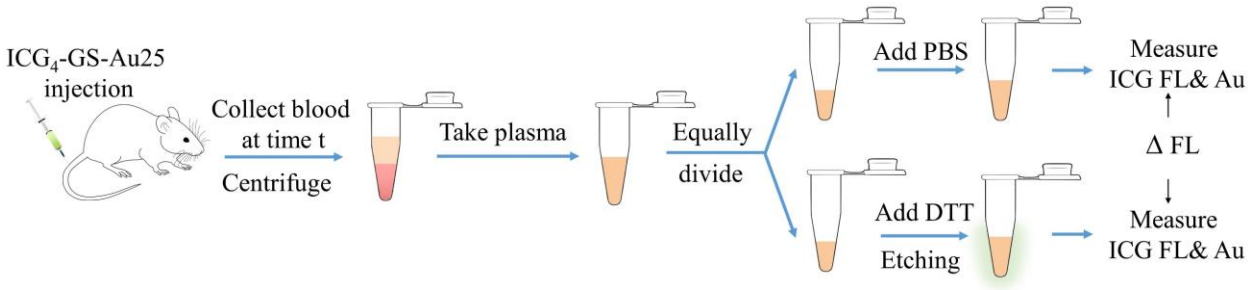

$$\text{Number of ICG on Au25 at time t} = 4.1\times\left(\frac{\Delta FL\ per\ Au\ at\ time\ t}{\Delta FL\ per\ Au\ at\ 0\ min}\right)$$

Supplementary Fig. 13. Scheme of quantifying the number of ICG molecules per circulating Au25 in blood.

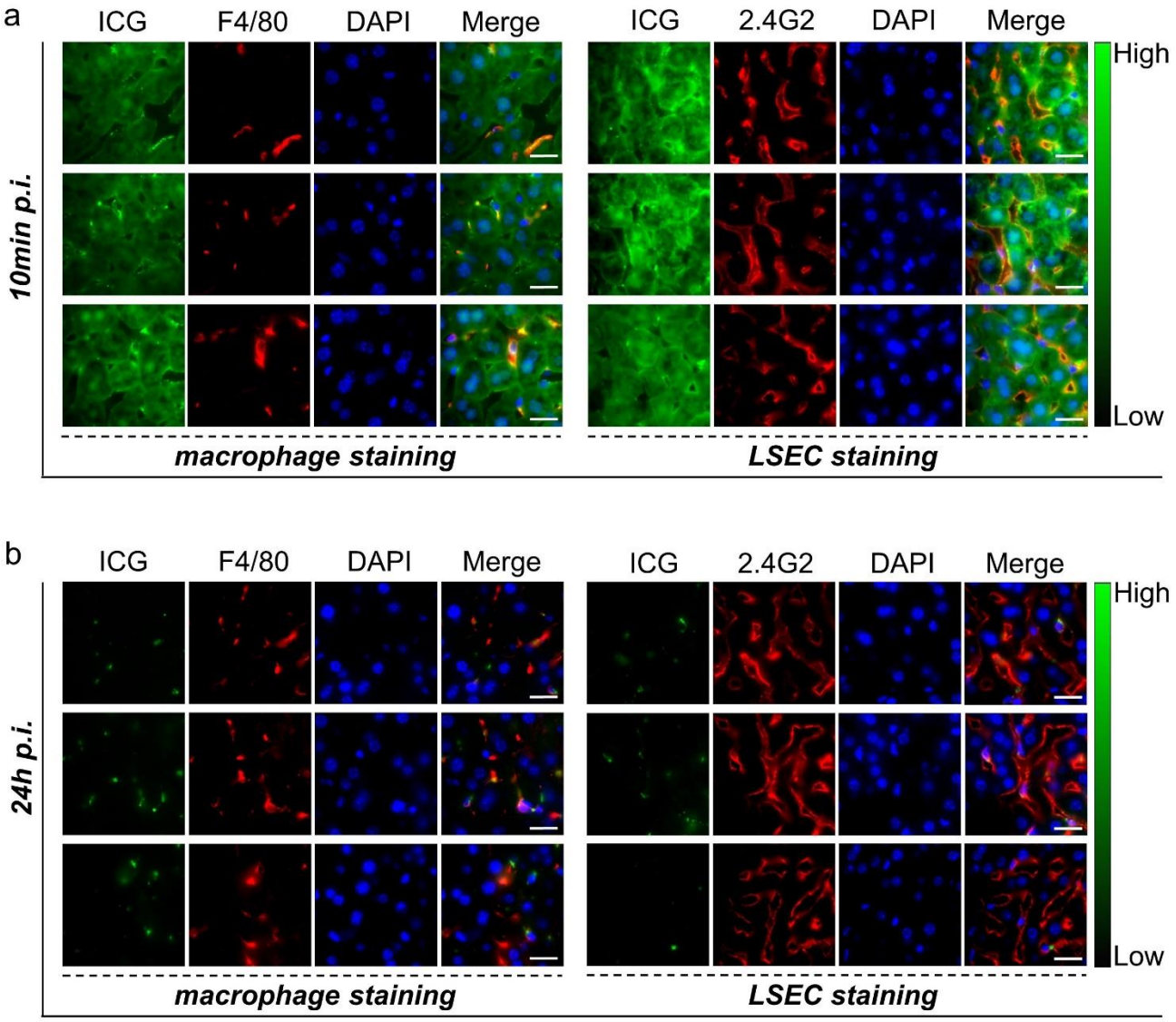

Supplementary Fig. 14. Fluorescent IHC staining of liver macrophage and liver sinusoidal endothelial cell (LESC). Fluorescent images of liver tissue slides with immunohistochemistry (IHC) staining of macrophage or LSEC from mice injected with ICG_4-GS-Au25 at 10 min (a) and 24 h (b) post injection. Cell nuclei were counterstained with DAPI. Scale bar, 15 μm. The bright and dotted ICG fluorescence around the wall of sinusoids had longer retention than those ICG signals in hepatocytes and colocalized well with either liver macrophage or LSEC, indicating that a very small portion of injected ICG_4-GS-Au25 was still subject to uptake by those scavenger cells in liver. These experiments were repeated twice with similar results.

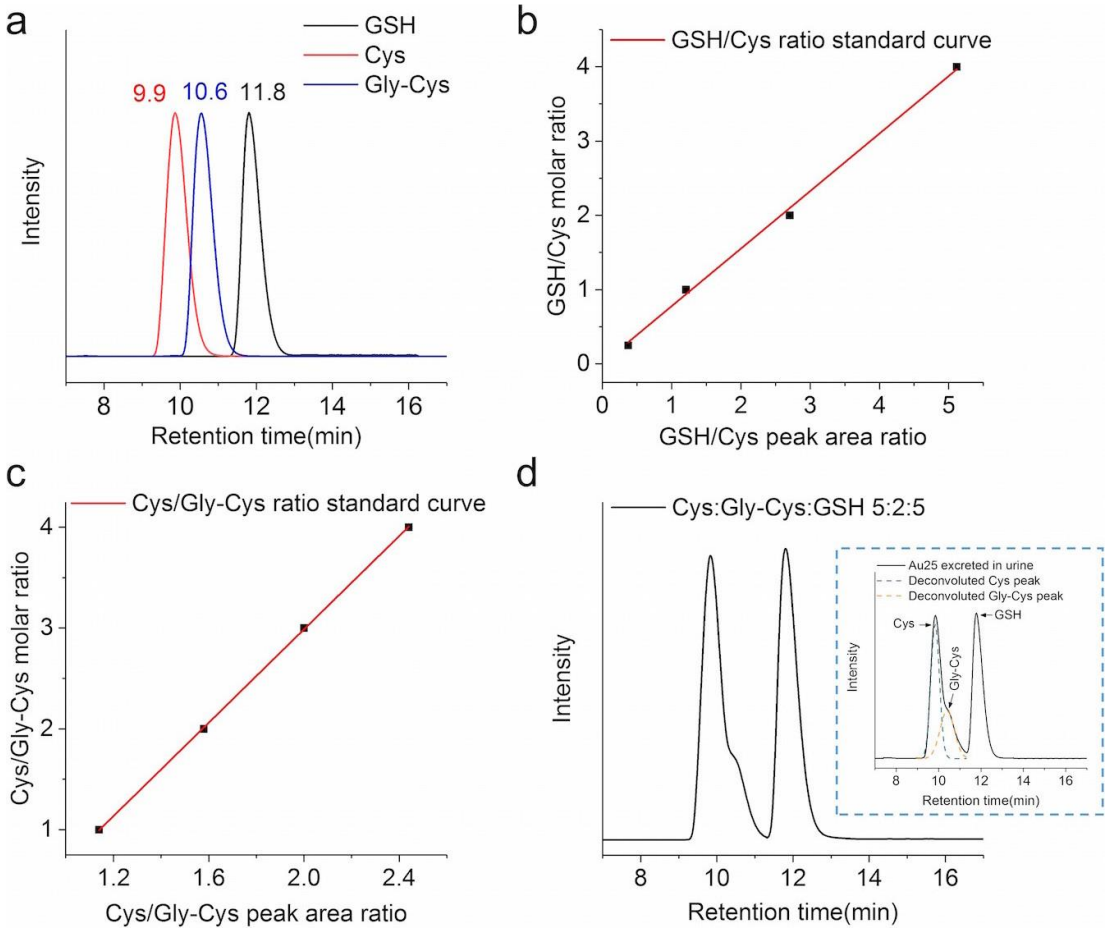

Supplementary Fig. 15. HPLC peak assignment and quantifications. (a), Retention times of NPM derivatized Cys (~9.9 min), Gly-Cys (~10.6 min) and GSH (~11.8 min) in HPLC under the same condition as that used for nanoparticle surface ligand analysis, matching well to the retention times of those surface ligands on the excreted Au25 in urine. (b), Standard curve of the GSH/Cys molar ratio versus their peak area ratio. (c), Standard curve of the Cys/Gly-Cys molar ratio versus their peak area ratio. (d), HPLC result of a mixture of Cys, Gly-Cys and GSH at a molar ratio of 5:2:5 (calculated based on the standard curves), which is almost identical to that obtained from the surface ligands of the excreted Au25 (inserted), further validated the peak assignment and quantifications. These experiments were repeated twice with similar results.

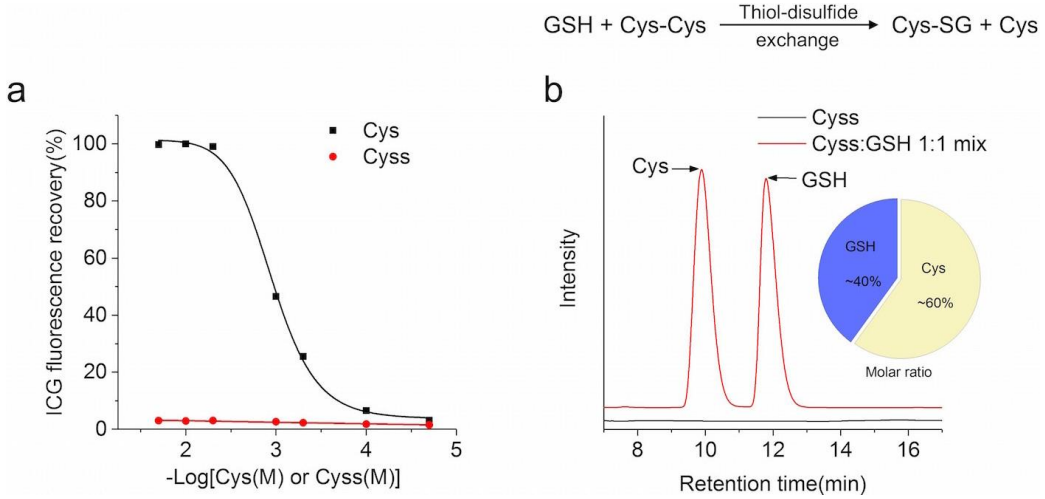

Supplementary Fig. 16. In vitro thiol-disulfide exchange between GSH and cystine. (a) Percentage of ICG fluorescence recovery after incubating ICG_4-GS-Au25 in PBS containing various concentrations of either cysteine (Cys) or cystine (Cyss) for 10 min at 37ºC. While Cys is able to displace ICG-GS from the surface of Au25 in a concentration dependent manner, Cyss cannot displace ICG-GS regardless of its concentration due to the absence of reduced thiol group (-SH). (b), HPLC results of pure Cyss and a 1:1 mixture of Cyss and GSH. The disulfide group in Cyss cannot react with NPM so no signal could be observed for pure Cyss; however, a 1:1 mixture of GSH and Cyss in PBS for just 5 min at 37ºC (pH 7.4) could rapidly convert ~ 60% Cyss to Cys via thiol-disulfide exchange reaction, consistent with the literature that GSH-Cyss reaction favors the formation of Cys (equilibrium constant k>1) in physiological conditions[3]. These experiments were repeated twice times with similar results.

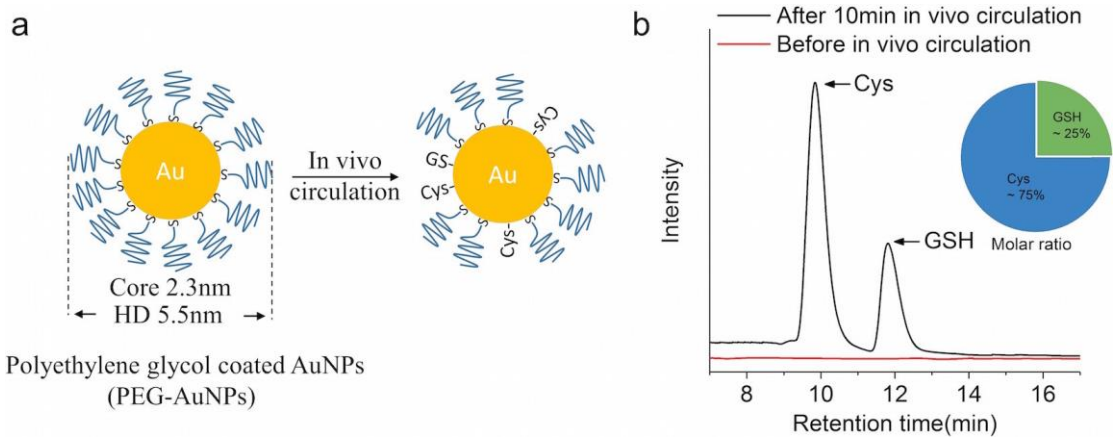

Supplementary Fig. 17. Surface ligand analysis of PEG-AuNPs after 10 min in vivo circulation. (a) Illustration of the PEG-AuNPs used for in vivo experiment. PEG-AuNPs were synthesized based on our previously reported method[2]. (b) HPLC analysis of the surface ligands of PEG-AuNPs before and after in vivo circulation. PEG-AuNPs were intravenously injected into mice immediately after their renal arteries were clamped to prevent renal elimination of PEG-AuNPs. After 10 min circulation, blood was withdrawn through cardiac puncture and PEG-AuNPs were extracted and purified for surface ligand analysis. GSH and Cys with a molar ratio of ~1:3 were found on the surface of PEG-AuNPs after in vivo circulation. Since ligand displacement of circulating AuNPs happened mainly at liver sinusoids, this experiment further confirmed the primary role of sinusoidal GSH and Cys in biotransforming the surface chemistry of circulating AuNPs in vivo. This experiment was repeated twice with similar results.

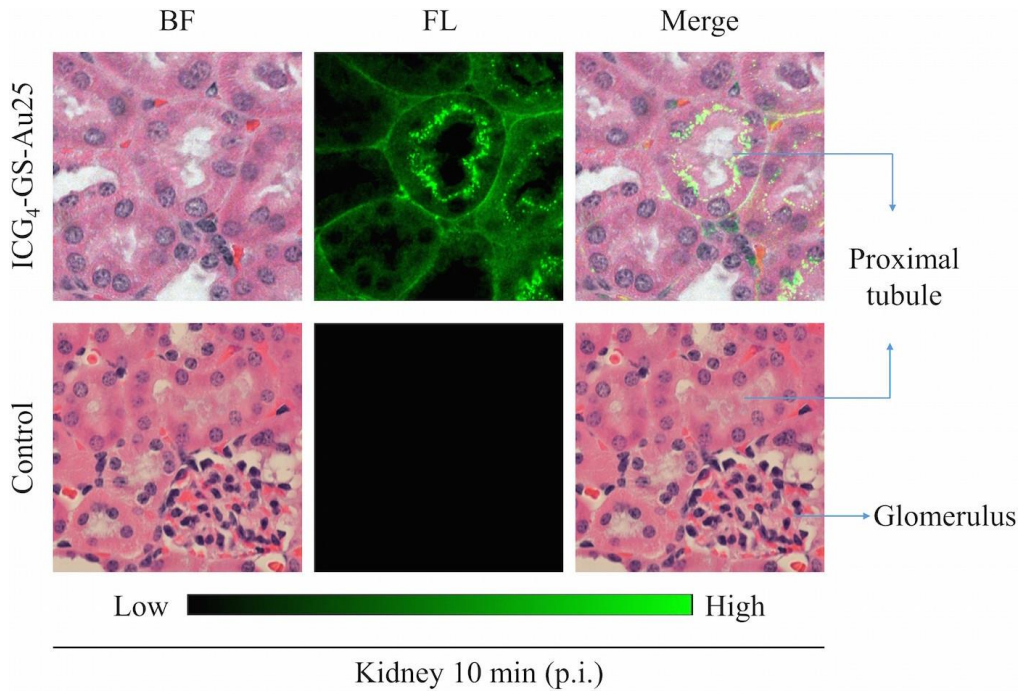

Supplementary Fig. 18. Additional fluorescence image of kidney tissue from ICG$_4$-GS-Au25 injected mice and the control. Control images are from mice injected with PBS. Scale bar, 20 μm. These experiments were repeated three times with similar results.

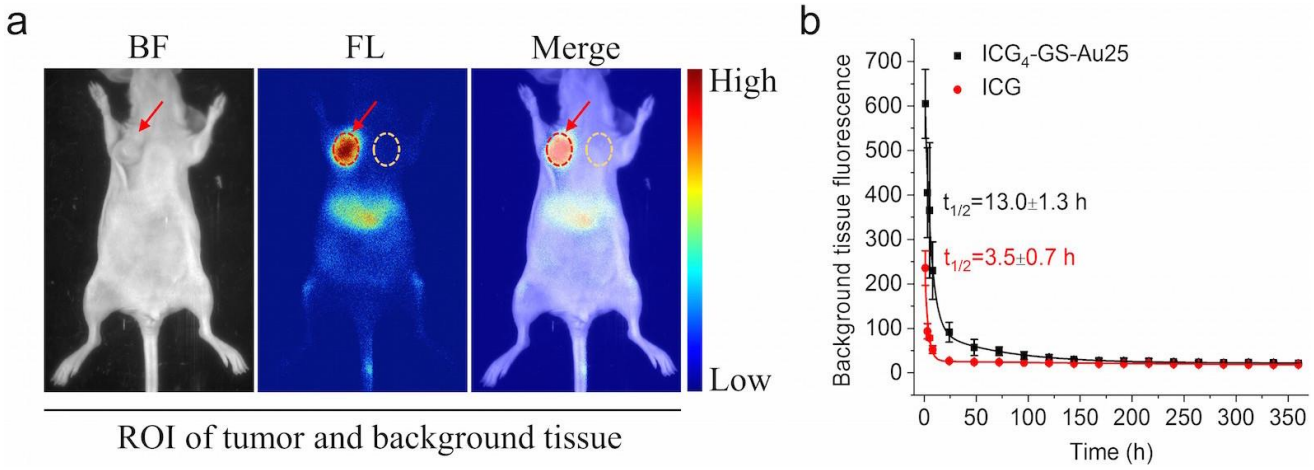

Supplementary Fig. 19. Decay of background tissue fluorescence signal over time. (a), Representative in vivo imaging of ICG$_4$-GS-Au25 injected mouse (72 h p.i.) illustrating the region of interest (ROI) chosen for tumor (red dashed circle) and background tissue (yellow dashed circle) ICG fluorescence quantification. Red arrows indicate tumor location. (b), Decay profiles of ICG fluorescence in background tissues over time for mice injected with ICG$_4$-GS-Au25 (n=3 mice) or free ICG (n=3 mice). These experiments were repeated twice with similar results. Data points indicate the mean with error bars representing the standard deviation.

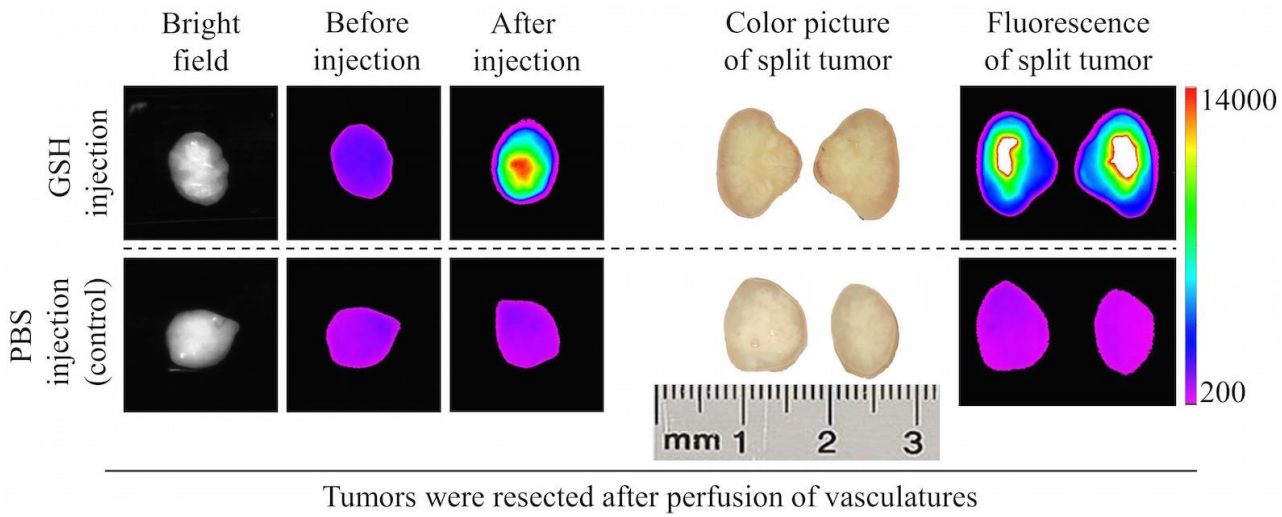

Supplementary Fig. 20. Intratumoral injection of GSH to release ICG from Au25 in tumor microenvironment. At 15 min post intravenous injection of ICG_4-GS-Au25, mice were sacrificed and thoroughly perfused with PBS to remove blood from vasculatures before the resection of tumors. Intratumoral injection of 10 mM GSH (pH adjusted to 7.4) could instantaneously light up the tumor by displacing ICG-GS from Au25 in tumor microenvironment whereas intratumor injection of PBS as the control cannot increase the ICG fluorescence in tumor. The fluorescence images of the split tumor (cut from the center into two pieces) show that ICG-Au25 conjugates had excellent tumor permeability and could infiltrate into tumor core rapidly after systemic administration. These experiments were repeated twice with similar results.

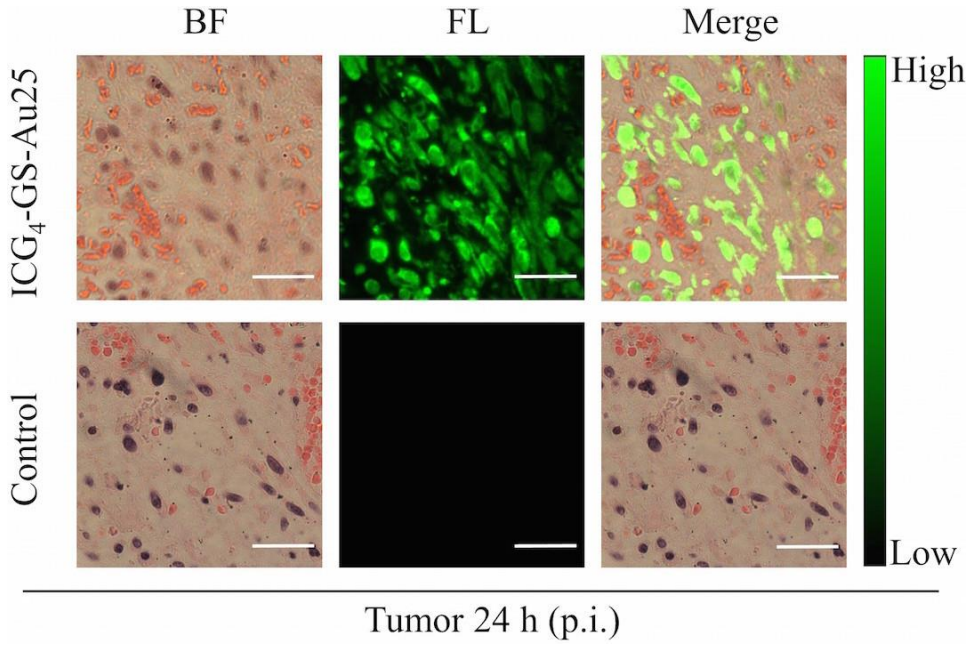

Supplementary Fig. 21. Additional fluorescence image of tumor tissue from ICG_4-GS-Au25 injected mice and the control. Control images are from mice injected with PBS. Scale bar, 20 μm. These experiments were repeated three times with similar results.

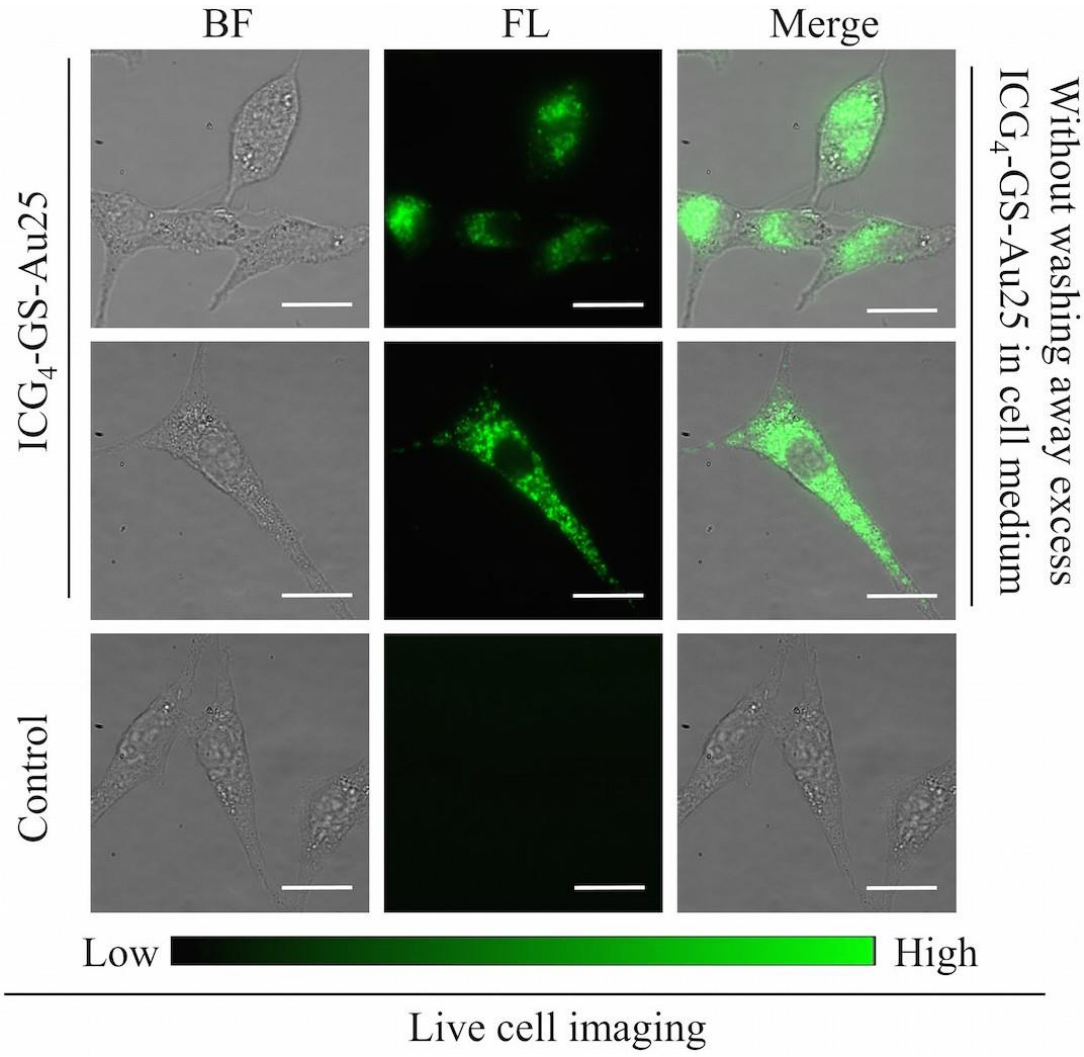

Supplementary Fig. 22. In vitro tumor cell uptake of ICG_4-GS-Au25. ICG_4-GS-Au25 was efficiently endocytosed by MCF-7 cells after 12 h incubation and located in endosome-like membrane-bound compartments inside cells, similar to that observed in in vivo tumor tissue slides. While ICG_4-GS-Au25 was non-fluorescent in cell culture medium, bright ICG fluorescence was observed once ICG_4-GS-Au25 entered tumor cells, suggesting that ICG dissociated from Au25 inside tumor cells, very likely due to the high concentration of intracellular GSH. Scale bar, 20 μm. These experiments were repeated four times with similar results.

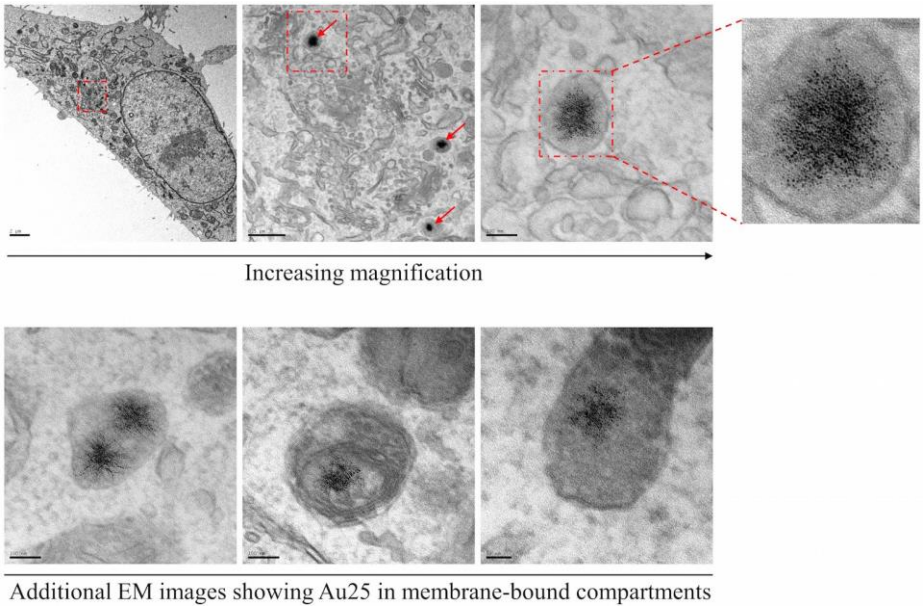

Supplementary Fig. 23. Electron microscope images of in vitro tumor cell uptake of ICG$_4$-GS-Au25. MCF-7 tumor cells were incubated with 1 M ICG$_4$-GS-Au25 in cell culture medium for 12 h before being fixed and embedded. AuNPs (indicated by red arrows) were taken up by the tumor cells and located in membrane-bound cellular compartments, in agreement with the fluorescence cell imaging result. This experiment was performed once.

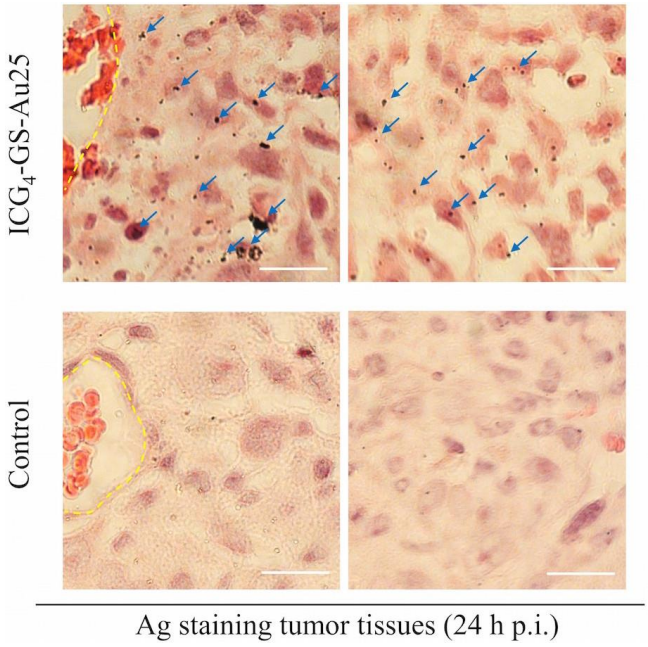

Supplementary Fig. 24. Silver staining of AuNPs in tumor tissues. Silver staining of the tumor tissues from ICG$_4$-GS-Au25 injected mice revealed that many AuNPs (pointed by blue arrows) were located in cells, indicating that ICG-Au25 conjugates effectively extravasated and penetrated into tumor interstitium and then were efficiently taken up by the cells in tumor. Control images show tumor slides from PBS injected mice underwent the same silver staining procedure. Yellow dashed line outlines the blood vessels. Scale bar, 10 μm. These experiments were repeated twice with similar results.

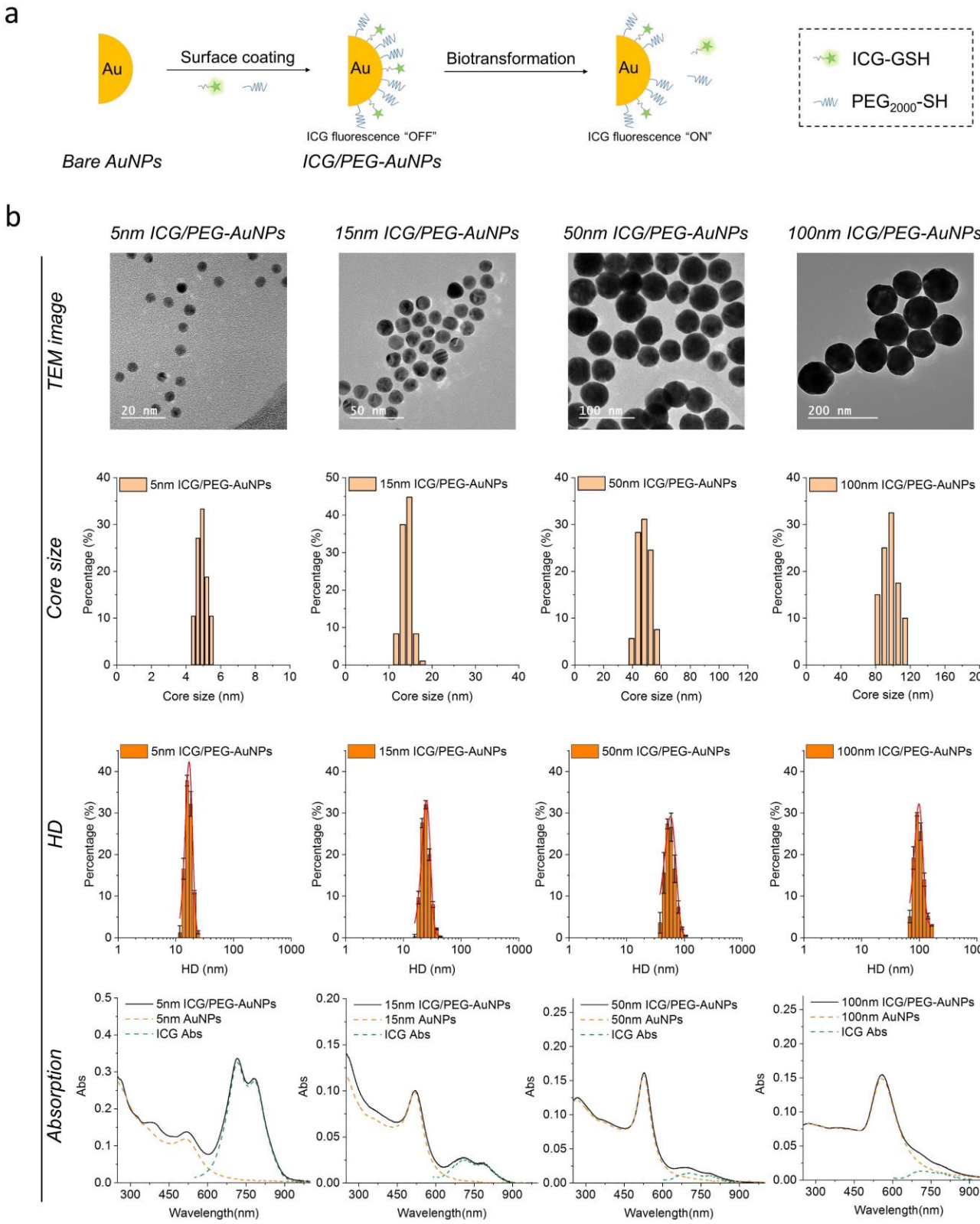
a
Au
Surface coating
Au
Biotransformation
Au
ICG-GSH
PEG2000-SH
ICG fluorescence "OFF"
ICG fluorescence "ON"
Bare AuNPs
ICG/PEG-AuNPs
b
5nm ICG/PEG-AuNPs
15nm ICG/PEG-AuNPs
50nm ICG/PEG-AuNPs
100nm ICG/PEG-AuNPs
TEM image
20 nm
50 nm
100 nm
200 nm
Core size
Percentage (%)
Core size (nm)
HD
HD (nm)
Absorption
5nm AuNPs
15nm AuNPs
50nm AuNPs
100nm AuNPs
ICG Abs
Abs
Wavelength(nm)

c

	5nm ICG/PEG-AuNPs	*15nm ICG/PEG-AuNPs*	*50nm ICG/PEG-AuNPs*	*100nm ICG/PEG-AuNPs*
Core size (nm)	4.9±0.3	14.1±1.2	48.1±4.7	96.3±9.3
Hydrodynamic diameter (HD, nm)	16.9±2.4	25.0±4.3	57.7±13.6	98.5±16.5
ICG coverage density (number of ICG/nm²)	~2.2	~1.1	~1.6	~2.6

d

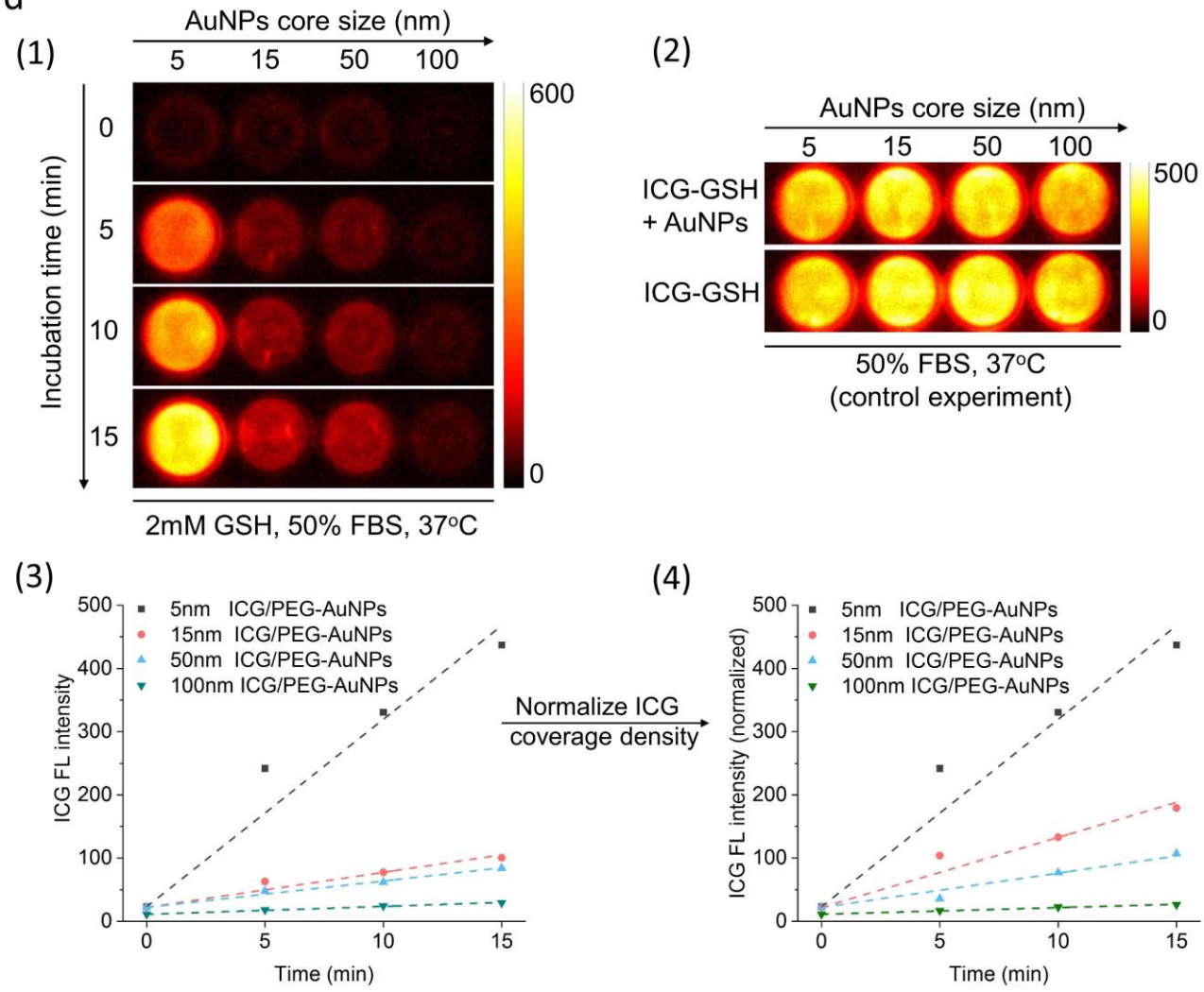

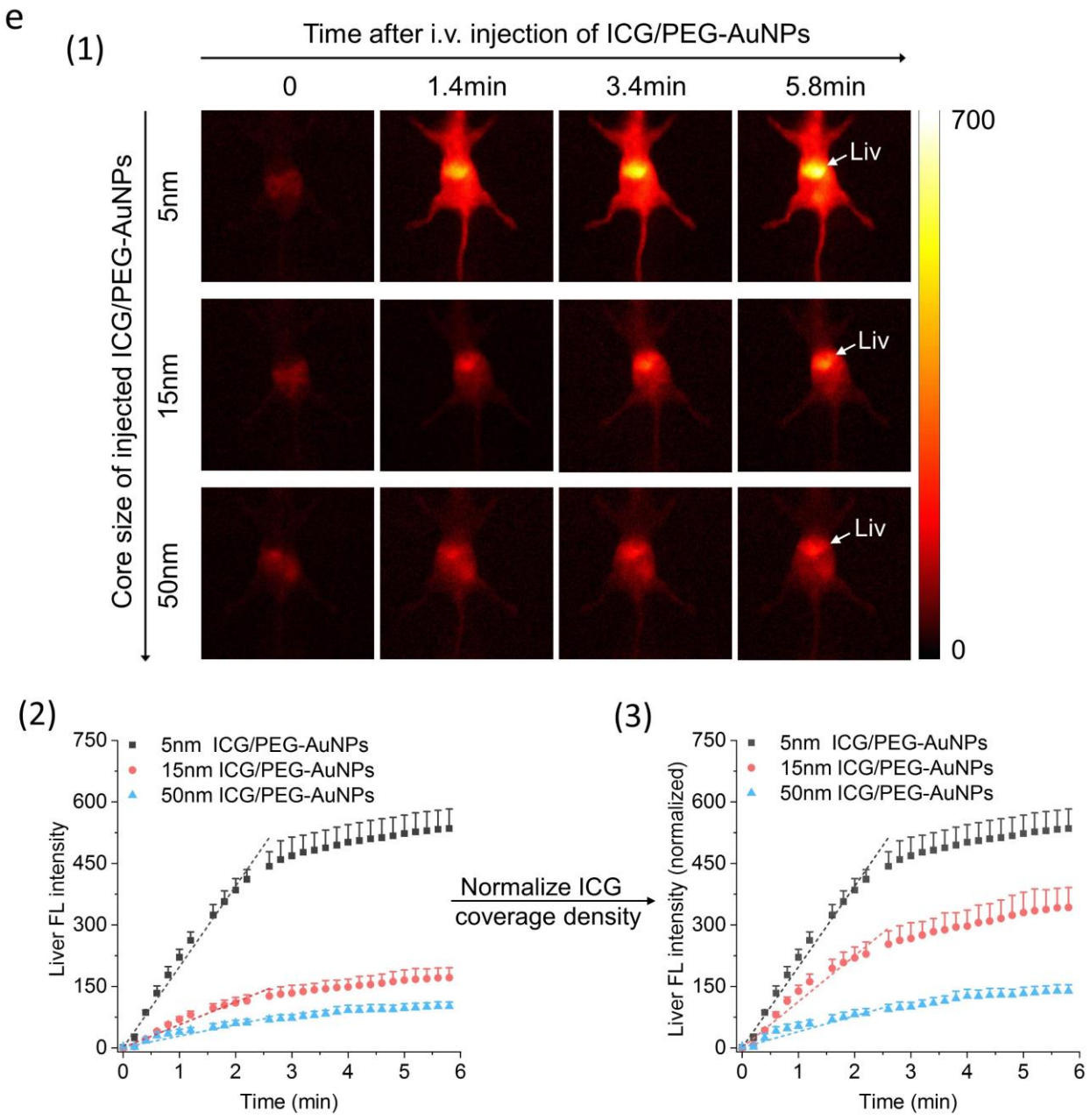
e
(1)
Time after i.v. injection of ICG/PEG-AuNPs
0
1.4min
3.4min
5.8min
Core size of injected ICG/PEG-AuNPs
5nm
15nm
50nm
Liv
Liv
Liv
700
0
(2)
5nm ICG/PEG-AuNPs
15nm ICG/PEG-AuNPs
50nm ICG/PEG-AuNPs
Liver FL intensity
Time (min)
Normalize ICG
coverage density
(3)
5nm ICG/PEG-AuNPs
15nm ICG/PEG-AuNPs
50nm ICG/PEG-AuNPs
Liver FL intensity (normalized)
Time (min)

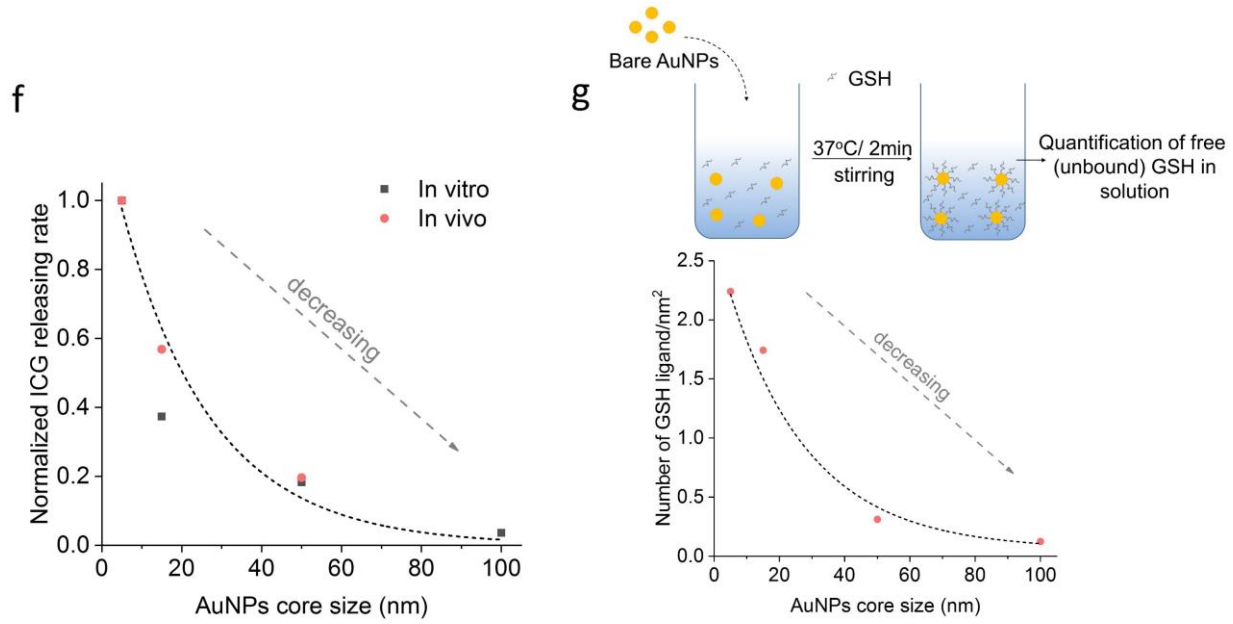

Supplementary Fig. 25. Glutathione-mediated biotransformation of different-sized AuNPs. (a) Scheme illustrating the construction of ICG/PEG-AuNPs and monitoring of glutathione-mediated biotransformation through the "turn-on" of ICG fluorescence. (b) Characterization of different-sized ICG/PEG-AuNPs (n=50 particles for core size quantification and n=3 measurements for DLS measurements). The subtraction-derived ICG absorption and the particle size were used to calculate the ICG surface coverage density on AuNPs. (c) Table summarizing the core size, hydrodynamic diameter and calculated ICG surface coverage density of different-sized ICG/PEG-AuNPs. Data are shown as mean ± sd. (d) 1) Fluorescence imaging of different-sized ICG/PEG-AuNPs incubated in 2mM GSH PBS solution (containing 50% FBS, 37°C, pH7.4) for 0, 5, 10 and 15 min. The total amount of ICG was kept the same for each sized ICG/PEG-AuNPs. 2) Control experiment showing that fluorescence of the released ICG-GSH would not be quenched by the different-sized AuNPs. 3,4) Time-dependent ICG fluorescence recovering rate of different-sized ICG/PEG-AuNPs before and after factoring differences in their surface ICG coverage density (all normalized to that of 5nm ICG/PEG-AuNPs). (e) 1) Representative noninvasive *in-vivo* fluorescence imaging of macrophage-depleted mice at multiple time points following intravenous injection of different-sized ICG/PEG-AuNPs. The total amount of injected ICG was kept the same for each sized ICG/PEG-AuNPs. 100nm ICG/PEG-AuNPs were excluded in the *in vivo* study due to enormous dose of AuNPs required to keep ICG amount constant for different-sized AuNPs and a decent S/N ratio as well. 2,3) Time-dependent liver ICG fluorescence intensity of mice injected with different-sized ICG/PEG-AuNPs before and after factoring differences in their surface ICG coverage density (all normalized to that of 5nm ICG/PEG-AuNPs), n=3 mice, data points indicate mean with error bars representing the standard deviation. (f) Normalized ICG releasing rate in both *in-vitro* and *in-vivo* experiments with respect to the size of ICG/PEG-AuNPs (after correction of their differences in ICG surface coverage density). Both *in-vitro* and *in-vivo* experiments indicate that biotransformation rate of solid AuNPs decrease exponentially with the increase in their core sizes. (g) Average GSH ligand density on different-sized bare (citrate-stabilized) AuNPs after reaction with excess GSH for just 2min. GSH reacts significantly faster with smaller bare AuNPs than that of larger ones even in the very beginning time period (the first 2 min) when GSH could almost freely react with AuNPs without much ligand-ligand steric hindrance , implying this size-dependent glutathione-mediated biotransformation arises fundamentally from the fact that the surface gold atoms of smaller AuNPs are more reactive towards GSH. The scheme on the top depicts the experimental design. GSH ligand density on nanoparticle surface was determined by quantifying the remaining free unbound GSH in solution after reaction through the Tietze enzymatic recycling assay. Measurements in figure b, d and g were repeated twice with similar results whereas other experiments were performed once with corresponding controls.

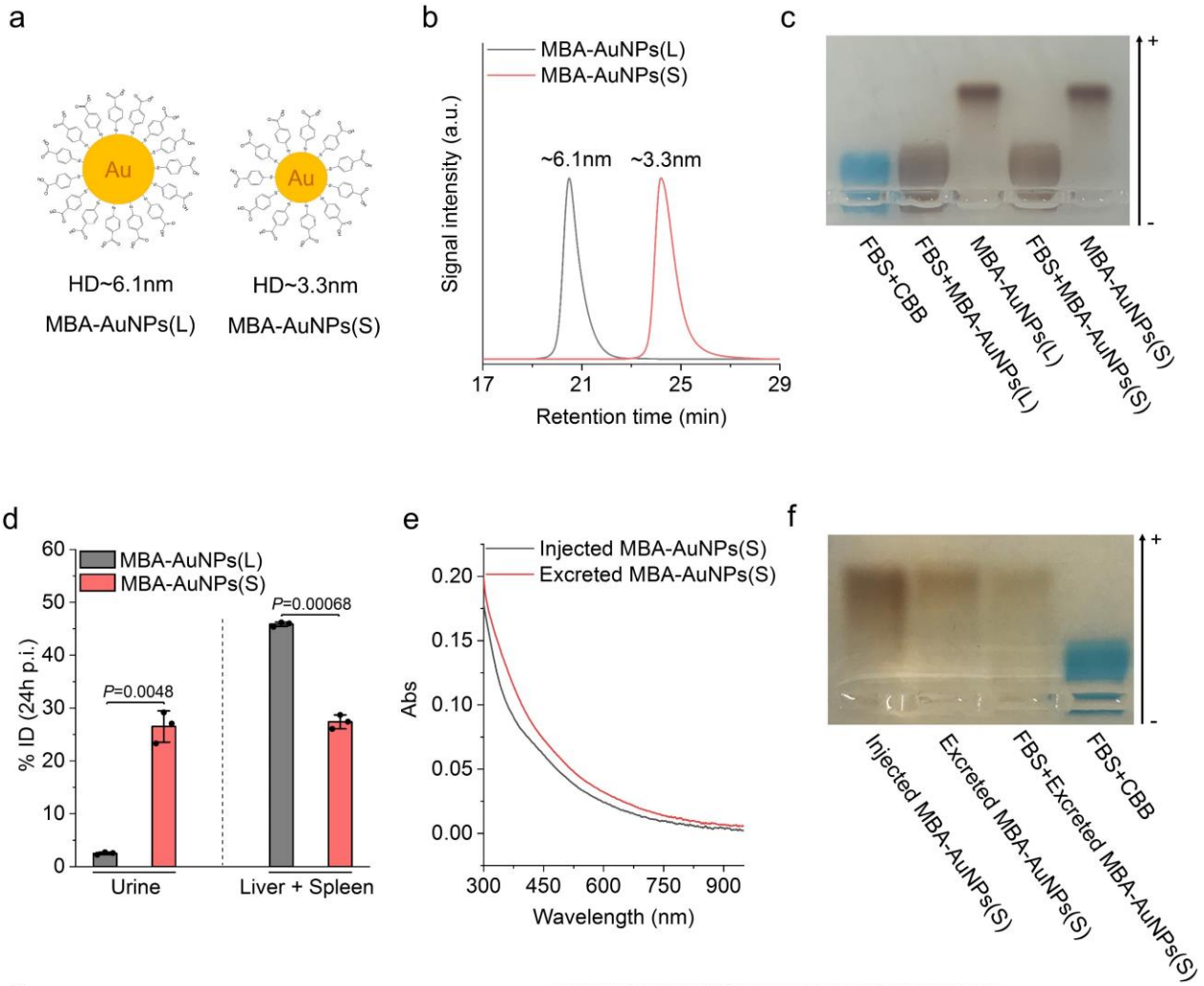
a
Au
Au
HD~6.1nm
MBA-AuNPs(L)
HD~3.3nm
MBA-AuNPs(S)
b
MBA-AuNPs(L)
MBA-AuNPs(S)
~6.1nm
~3.3nm
Signal intensity (a.u.)
17
21
25
29
Retention time (min)
c
+
-
FBS+CBB
FBS+MBA-AuNPs(L)
MBA-AuNPs(L)
FBS+MBA-AuNPs(S)
MBA-AuNPs(S)
d
MBA-AuNPs(L)
MBA-AuNPs(S)
% ID (24h p.i.)
P=0.0048
P=0.00068
Urine
Liver + Spleen
e
Injected MBA-AuNPs(S)
Excreted MBA-AuNPs(S)
Abs
Wavelength (nm)
f
+
-
Injected MBA-AuNPs(S)
Excreted MBA-AuNPs(S)
FBS+Excreted MBA-AuNPs(S)
FBS+CBB
g
In vivo
circulation
Enter
liver
Liver
Glutathione-mediated
biotransformation
Competing
MPS
uptake
MPS uptake
Kidney
elimination
Scavenger cells
Large
MBA-AuNPs
Serum proteins
Small
MBA-AuNPs
GSH/Cysteine

Supplementary Fig. 26. Glutathione-mediated biotransformation of 3nm and 6nm 4-mercaptobenzoic acid coated gold nanoparticles (MBA-AuNPs). (a) Two different-sized MBA-AuNPs were synthesized and named as MBA-AuNPs(L) for the larger ones and MBA-AuNPs(S) for the smaller ones. (b) Gel filtration chromatography of the two different-sized MBA-AuNPs. Their sizes were determined by a series of protein standards. (c) Due to the lack of antifouling property of MBA ligand, both MBA-AuNPs bind to serum proteins tightly as revealed by the agarose gel electrophoresis. (d) Au accumulation in urine as well as in liver and spleen of mice at 24h post intravenous injection of MBA-AuNPs(L) or MBA-AuNPs(S), n=3 mice. MBA-AuNPs(S) exhibited a 10-fold increase in renal clearance and significantly lowered MPS uptake compared to that of MBA-AuNPs(L) at 24h p.i. Column values indicate the mean with error bars representing the standard deviation. Statistical significance is evaluated by two-sample unequal variances (Welch's) t-test. (e) The MBA-AuNPs (S) excreted in urine had similar absorption of the Au cores relative to the injected ones, indicating that their Au core structures didn't change. (f) The MBA-AuNPs (S) excreted in urine were found to no longer bind to serum proteins, clearly proving that their surface chemistry had been biotransformed. (g) Scheme illustrating the competing and interacting role of hepatic GSH-mediated biotransformation and MPS uptake in modulating the in-vivo transport of both MBA-AuNPs. These results clearly confirmed the balance between MPS uptake and glutathione-mediated biotransformation and that smaller MBA-AuNPs were more readily transformed by the glutathione-mediated biotransformation, which significantly enhanced their renal clearance and reduced nonspecific accumulation by the MPS than that of larger MBA-AuNPs, consistent with our observation from ICG_4-GS-Au25 and other large AuNPs. Protein binding experiments in figure c and f were repeated twice with similar results whereas other experiments were performed once with corresponding controls.

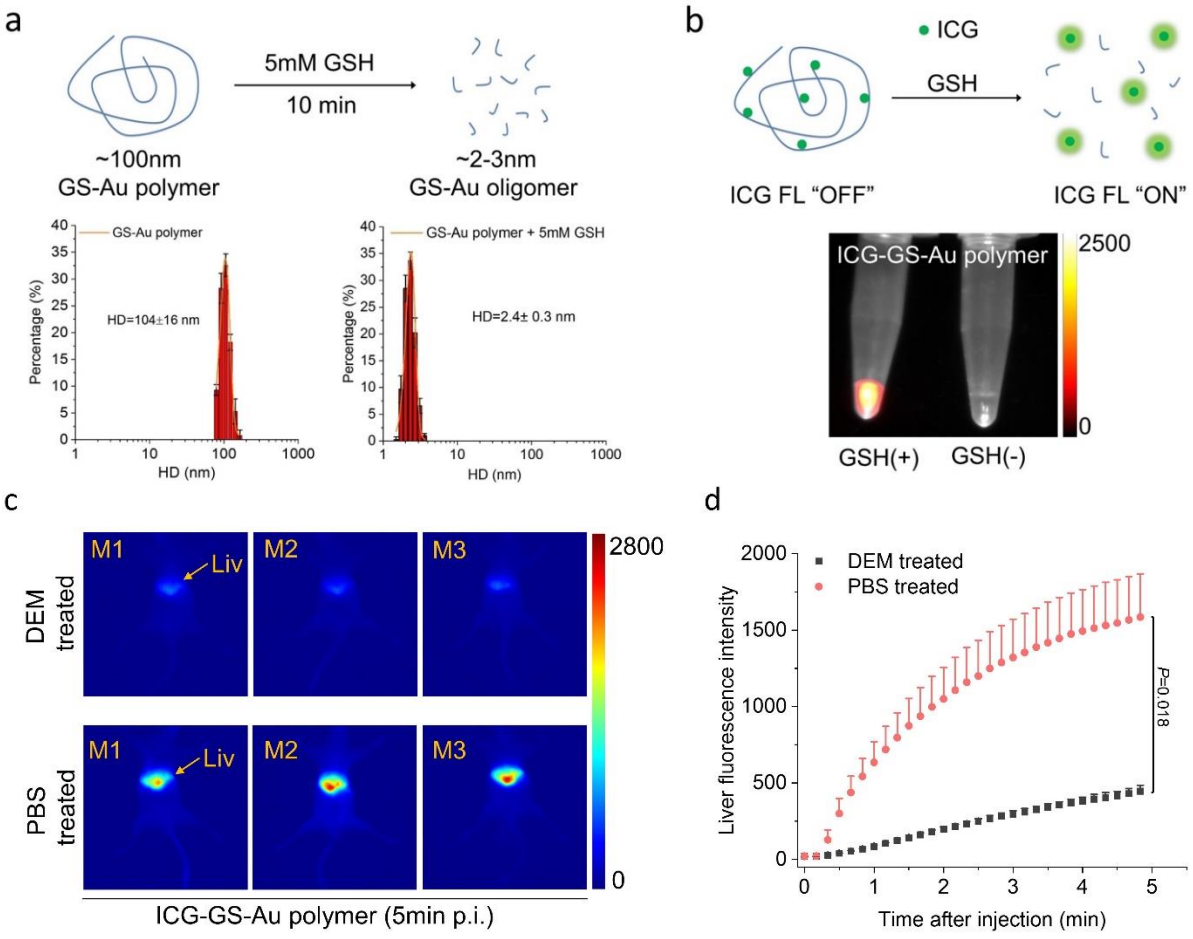

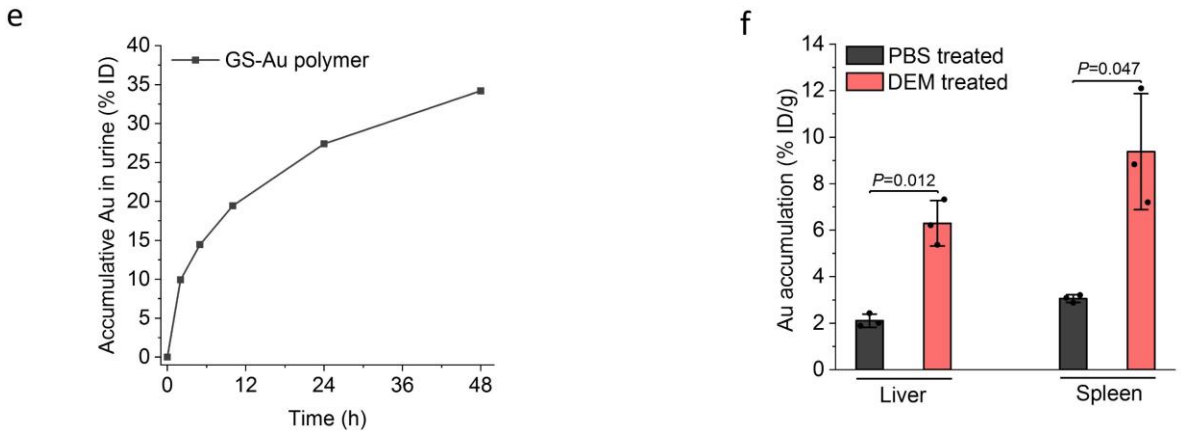

Supplementary Fig. 27. Glutathione-mediated biotransformation of ~100nm polymeric GS-Au nanoparticles. (a) Scheme showing that ~100 nm large GS-Au polymeric nanoparticles could be disintegrated into ~2-3 nm ultrasmall nanoparticles after incubation with 5mM GSH PBS solution (37ºC, pH7.4) for 10min as proved by DLS measurement (n=3 measurements) of their hydrodynamic diameter (HD). (b) Illustration of ICG conjugated GS-Au polymeric nanoparticles (ICG-GS-Au polymer) and the "turn-on" of ICG fluorescence when ICG-GS-Au polymer were dissociated by GSH. Shown in the bottom is the fluorescence image of ICG-GS-Au polymer in PBS solution with (+) and without (-) 5mM GSH (pH7.4). (c) Noninvasive *in-vivo* fluorescence imaging of mice treated with either DEM (n=3 mice) or PBS (n=3 mice) at 5min post intravenous injection of the same ICG-GS-Au polymer. (d) Time-dependent liver ICG fluorescence intensity of DEM- and PBS-treated mice (n=3) following i.v. injection of the same ICG-GS-Au polymer. Liver ICG fluorescence in control mice (PBS-treated) increased significantly faster than that in DEM-treated mice, clearly proving that the polymeric GS-Au nanoparticles were disintegrated by the glutathione-mediated biotransformation in liver. (e) Renal clearance of the ~100 nm GS-Au polymer through the *in vivo* dissociation in liver during the first 48h p.i. (f) Liver and spleen accumulation of Au in DEM- and PBS-treated mice (n=3) at 48h post intravenous injection of the same GS-Au polymer. The liver and spleen accumulation of polymeric GS-Au nanoparticles significantly increased once mice were pretreated with DEM to inhibit glutathione-mediated biotransformation, consistent with our hypothesis that glutathione-mediated biotransformation helps to facilitate the renal clearance of GS-Au polymer and reduce the MPS uptake. Statistical significance is evaluated by two-sample unequal variances (Welch's) t-test. Centre values indicate the mean with error bars representing the standard deviation. Measurements in figure a and b were repeated twice whereas other experiments were performed once with corresponding controls.

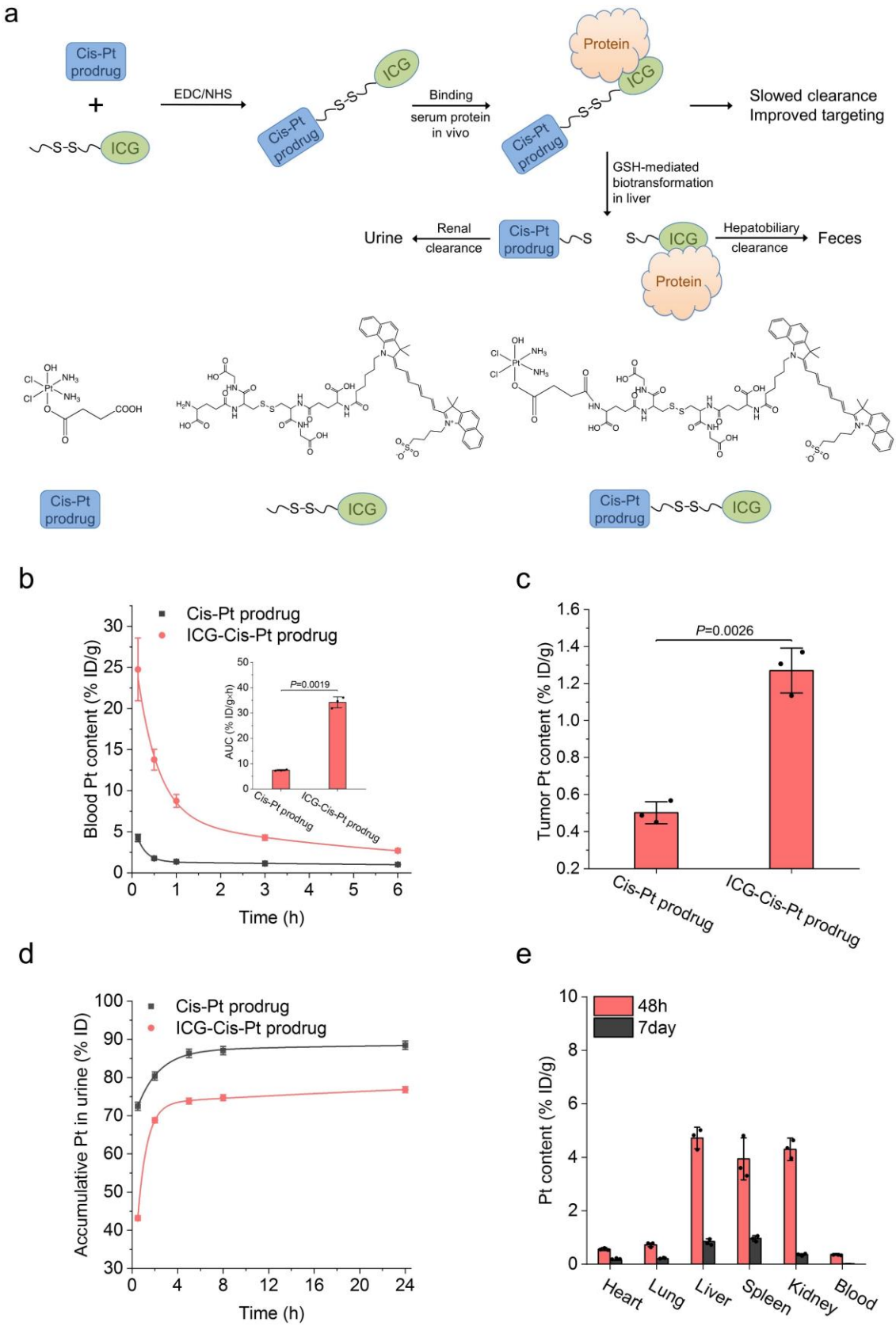
a
Cis-Pt prodrug
EDC/NHS
ICG
Binding serum protein in vivo
Protein
Slowed clearance
Improved targeting
GSH-mediated biotransformation in liver
Urine
Renal clearance
Hepatobiliary clearance
Feces
b
Cis-Pt prodrug
ICG-Cis-Pt prodrug
Blood Pt content (% ID/g)
Time (h)
P=0.0019
AUC (% ID/g×h)
c
P=0.0026
Tumor Pt content (% ID/g)
d
Accumulative Pt in urine (% ID)
e
48h
7day
Pt content (% ID/g)
Heart
Lung
Liver
Spleen
Kidney
Blood

Supplementary Fig. 28. Utilization of hepatic glutathione-mediated biotransformation to enhance tumor targeting of a cisplatin prodrug. (a)Scheme illustrating the rationale of designing the ICG-Cis-Pt prodrug by combining temporal serum protein binding and hepatic glutathione-mediated biotransformation to slow down the rapid renal clearance of Cis-Pt prodrug and enhance its tumor targeting efficiency while avoiding predominant accumulation in MPS. (b) Blood retention of ICG-Cis-Pt prodrug (n=3 mice) is significantly longer than that of Cis-Pt prodrug (n=3 mice) due to ICG-induced serum protein binding that slows down the renal clearance. Inserted is the comparison of AUC of ICG-Cis-Pt prodrug (34.2±2.2 % ID/g×h) and that of Cis-Pt prodrug (7.4±0.2 % ID/g×h) during the first 6h p.i.. (c)Tumor targeting efficiency of Cis-Pt prodrug (n=3 mice) and ICG-Cis-Pt prodrug (n=3 mice) at 48h p.i. (d) Renal clearance profiles of Cis-Pt prodrug and ICG-Cis-Pt prodrug (n=3 measurements). The initial renal clearance kinetics of ICG-Cis-Pt is significantly reduced relative to that of Cis-Pt prodrug, consistent with the pharmacokinetics study. (e) Biodistribution of Pt in organs at 48 h and 7 day following intravenously injection of ICG-Cis-Pt prodrug (n=3 mice). The accumulation of ICG-Cis-Pt in MPS as well as in other major organs is low and continues to decrease over time. Statistical significance is evaluated by two-sample unequal variances (Welch's) t-test. Centre values indicate the mean with error bars representing the standard deviation. These experiments were performed once with corresponding controls.

3. Supplementary Movies

3.1 Noninvasive in vivo fluorescence imaging of ICG_4-GS-Au25 in PBS-treated and DEM-treated mice. These experiments were repeated more than five times with similar results.

4. Supplementary References

1 Wu, Z., Chen, J. & Jin, R. One-Pot Synthesis of Au25 (SG) 18 2-and 4-nm Gold Nanoparticles and Comparison of Their Size-Dependent Properties. *Adv. Funct. Mater.* **21**, 177-183 (2011).

2 Liu, J. *et al.* PEGylation and Zwitterionization: Pros and Cons in the Renal Clearance and Tumor Targeting of Near-IR-Emitting Gold Nanoparticles. *Angew. Chem.* **125**, 12804-12808 (2013).

3 Jocelyn, P. The Standard Redox Potential of Cysteine-Cystine from the Thiol-Disulphide Exchange Reaction with Glutathione and Lipoic Acid. *The FEBS Journal* **2**, 327-331 (1967).

4 Wu, Z., Suhan, J. & Jin, R. One-pot synthesis of atomically monodisperse, thiol-functionalized Au 25 nanoclusters. *J. Mater. Chem.* **19**, 622-626 (2009).

5 Dhar, S., Daniel, W. L., Giljohann, D. A., Mirkin, C. A. & Lippard, S. J. Polyvalent oligonucleotide gold nanoparticle conjugates as delivery vehicles for platinum (IV) warheads. *Journal of the American Chemical Society* **131**, 14652-14653 (2009).

6 Weber, C. A., Duncan, C. A., Lyons, M. J. & Jenkinson, S. G. Depletion of tissue glutathione with diethyl maleate enhances hyperbaric oxygen toxicity. *American Journal of Physiology-Lung Cellular and Molecular Physiology* **258**, L308-L312 (1990).

7 Adams, J., Lauterburg, B. & Mitchell, J. Plasma glutathione and glutathione disulfide in the rat: regulation and response to oxidative stress. *J. Pharmacol. Exp. Ther.* **227**, 749-754 (1983).

8 Rahman, I., Kode, A. & Biswas, S. K. Assay for quantitative determination of glutathione and glutathione disulfide levels using enzymatic recycling method. *Nature protocols* **1**, 3159 (2006).

9 Winters, R. A., Zukowski, J., Ercal, N., Matthews, R. H. & Spitz, D. R. Analysis of glutathione, glutathione disulfide, cysteine, homocysteine, and other biological thiols by high-performance liquid chromatography following derivatization by n-(1-pyrenyl) maleimide. *Anal. Biochem.* **227**, 14-21 (1995).